The Astrophysical Journal, 936:168 (16pp), 2022 September 10 https://doi.org/10.3847/1538-4357/ac87a6

Do All Low-Mass Stars Undergo Extra Mixing Processes?

Dana S. Balser[1], Trey V. Wenger[2], and T. M. Bania[3]
[1] National Radio Astronomy Observatory, 520 Edgemont Rd., Charlottesville, VA 22903, USA; dbalser@nrao.edu
[2] Dominion Radio Astrophysical Observatory, Herzberg Astronomy and Astrophysics Research Centre, National Research Council, P.O. Box 248, Penticton, BC V2A 6J9, Canada
[3] Institute for Astrophysical Research, Astronomy Department, Boston University, 725 Commonwealth Avenue, Boston, MA 02215, USA
Received 2022 April 27; revised 2022 August 4; accepted 2022 August 5; published 2022 September 12

Abstract

Standard stellar evolution models that only consider convection as a physical process to mix material inside of stars predict the production of significant amounts of ^{3}He in low-mass stars ($M < 2\,M_\odot$), with peak abundances of $^3\mathrm{He/H} \sim \text{few} \times 10^{-3}$ by number. Over the lifetime of the Galaxy, this ought to produce ^{3}He/H abundances that diminish with increasing Galactocentric radius. Observations of $^3\mathrm{He}^+$ in H II regions throughout the Galactic disk, however, reveal very little variation in the ^{3}He abundance with values of ^{3}He/H similar to the primordial abundance, $(^3\mathrm{He/H})_p \sim 10^{-5}$. This discrepancy, known as the "^{3}He problem," can be resolved by invoking in stellar evolution models an extra mixing mechanism due to the thermohaline instability. Here we observe $^3\mathrm{He}^+$ in the planetary nebula (PN) J320 (G190.3–17.7) with the Jansky Very Large Array to confirm a previous $^3\mathrm{He}^+$ detection made with the Very Large Array that supports standard stellar yields. This measurement alone indicates that not all stars undergo extra mixing. Our more sensitive observations do not detect $^3\mathrm{He}^+$ emission from J320 with an rms noise of 58.8 μJy beam^{-1} after smoothing the data to a velocity resolution of 11.4 km s^{-1}. We estimate an abundance limit of $^3\mathrm{He/H} \leqslant 2.75 \times 10^{-3}$ by number using the numerical radiative transfer code NEBULA. This result nullifies the last significant detection of $^3\mathrm{He}^+$ in a PN and allows for the possibility that all stars undergo extra mixing processes.

Unified Astronomy Thesaurus concepts: Stellar evolution (911); Planetary nebulae (1249); Radio spectroscopy (1359)

1. Background

The ^{3}He isotope is one of the few elements that not only is produced several minutes after the big bang during the era of primordial nucleosynthesis but also is subsequently made inside stars via stellar nucleosynthesis (e.g., Boesgaard & Steigman 1985). Measurements of ^{3}He therefore provide a unique probe of cosmic evolution. Rood et al. (1976) first identified the significance of measuring the ^{3}He abundance in the interstellar medium (ISM). They predicted an enrichment of the primordial ^{3}He abundance due to stellar nucleosynthesis based on ^{3}He yields from low-mass stars ($M < 2\,M_\odot$). Rood et al. (1976) argued that (1) the present-day ISM ^{3}He/H abundance ratio should be significantly larger than the protosolar value, (2) ^{3}He/H should grow with source metallicity, and (3) there should be a radial gradient in ^{3}He/H abundance across the Milky Way disk with higher abundances in the more processed central regions.

Detection of ^{3}He has proven challenging, however, since there is expected to be about one ^{3}He atom for every 10,000 ^{4}He atoms. Isotopic shifts for light elements are small compared with typical line widths, so using He recombination lines (e.g., He I λ6678) to detect ^{3}He is difficult. Nevertheless, anomalously high ^{3}He/H abundance ratios have been detected with He recombination lines in some stars (e.g., Sargent & Jugaku 1961). These very high ^{3}He abundances are thought to be due to diffusion and are therefore not representative of typical abundances. There have also been anomalously high ^{3}He/H abundances detected from in situ measurements of solar energetic particle events (e.g., Wiedenbeck et al. 2020). Potential molecular transitions including ^{3}He are rare since helium is inert and seldom found in molecular form. Detection of HeH^+ in the planetary nebula (PN) NGC 7027 is a recent exception (Güsten et al. 2019).

Townes (1957) was the first to suggest the $^3\mathrm{He}^+$ hyperfine transition at 8665.650 MHz (Novick & Cummins 1958) as a possible astrophysical tracer at radio frequencies. Goldwire & Goss (1967) calculated the Einstein coefficient of the $^3\mathrm{He}^+$ hyperfine transition, corresponding to a relatively short radiative lifetime of 16,000 yr, indicating the plausibility of measuring ^{3}He in H II regions (see also Syunyaev 1966). Initial attempts at detecting $^3\mathrm{He}^+$ in H II regions were unsuccessful and limited by high receiver system temperatures (Seling & Heiles 1969; Predmore et al. 1971).

Rood et al. (1979) made the first detection of ^{3}He in the ISM toward the giant H II region W51 with the Max-Planck Institut für Radioastronomie (MPIfR) 100 m telescope. They derived a ^{3}He/H abundance ratio similar to the protosolar value and thus found no evidence for the production of ^{3}He in low-mass stars. Observations of $^3\mathrm{He}^+$ in H II regions over the past four decades have yielded similar results—stars are not significant producers of ^{3}He (Rood et al. 1984; Bania et al. 1987; Balser et al. 1994; Bania et al. 1997; Balser & Bania 2018).

Accurate determination of the ^{3}He/H abundance ratio, the astrophysical quantity of interest, requires models of the density and ionization structure of the H II region. This is because the tracer of ^{3}He, the hyperfine transition, is sensitive to $\int n_e\,d\ell$, whereas the tracer of H, the free–free continuum, is sensitive to $\int n_e^2\,d\ell$ (Balser et al. 1999a). Here n_e is the electron density and $d\ell$ is the path length across the H II region.

Ionization structure is important because H and He have different ionization potentials (Bania et al. 2007). Using this information, Bania et al. (2002) selected sources with simple morphologies that would produce the most accurate ^{3}He/H abundance ratios and found that ^{3}He/H was approximately constant across the Galactic disk—"the ^{3}He plateau." They suggested that the ^{3}He plateau abundance of $^3\mathrm{He/H} = (1.1 \pm 0.2) \times 10^{-5}$ by number is the primordial abundance. This was later confirmed by combining results from the Wilkinson Microwave Anisotropy Probe (WMAP) with big bang nucleosynthesis (BBN) models yielding a primordial abundance of $(^3\mathrm{He/H})_p = (1.00 \pm 0.07) \times 10^{-5}$ (Romano et al. 2003; Cyburt et al. 2008).

Since low-mass stars were expected to be sources of ^{3}He enrichment to the ISM via mass loss during the asymptotic giant branch (AGB) phase, similar efforts were made to detect ^{3}He$^+$ in PNe. Rood et al. (1992) made the first detection of ^{3}He$^+$ in the PN NGC 3242 with the MPIfR 100 m (see also Balser et al. 1997, 1999b). They derived an abundance of $^3\mathrm{He/H} \gtrsim 10^{-3}$, two orders of magnitude larger than abundances found in H II regions, consistent with standard stellar models. Observations of ^{3}He$^+$ were made for a handful of PNe over the next two decades (Balser et al. 1997, 1999b, 2006; Guzman-Ramirez et al. 2013, 2016; Bania & Balser 2021). ^{3}He$^+$ detections were also claimed in PNe J320 (Balser et al. 2006) and IC 418 (Guzman-Ramirez et al. 2016) with derived abundance ratios of $^3\mathrm{He/H} \sim$ few $\times 10^{-3}$. So there seemed to be solid evidence that some low-mass stars were producing copious amounts of ^{3}He to be returned to the ISM during the PN phase.

Galactic chemical evolution (GCE) models using ^{3}He yields from standard stellar evolution predict significantly larger ^{3}He abundances over the lifetime of the Milky Way than are observed in H II regions (Galli et al. 1995; Olive et al. 1995; Galli et al. 1997). Most GCE models also predict negative radial ^{3}He/H abundance ratio gradients within the Galactic disk because the central regions have undergone more stellar processing than the outer regions over the lifetime of the Milky Way. This is inconsistent with the ^{3}He plateau revealed by observations. Moreover, in situ measurements of helium within the Jovian atmosphere with the Galileo probe yield $^3\mathrm{He}/^4\mathrm{He} = (1.66 \pm 0.05) \times 10^{-4}$ (Mahaffy et al. 1998). This corresponds to a protosolar abundance of $^3\mathrm{He/H} = (1.5 \pm 0.2) \times 10^{-5}$, indicating very little production of ^{3}He over the past 4.5 Gyr. Galli et al. (1997) called these discrepancies "the ^{3}He problem."

Rood et al. (1984) suggested that some sort of mixing could be taking place in low-mass stars that might explain the lower observed ^{3}He abundances than expected in the ISM. They posited that such a mixing mechanism may be related to the destruction of ^{7}Li in main-sequence stars and low $^{12}\mathrm{C}/^{13}\mathrm{C}$ abundance ratios observed in low-mass red giant branch (RGB) stars (see also Charbonnel 1995; Hogan 1995; Weiss et al. 1996). Numerous studies indicate that some sort of extra mixing is occurring when low-mass stars reach the luminosity bump on the RGB (e.g., Gilroy 1989; Luck 1994; Charbonnel et al. 1998; Gratton et al. 2000; Pilachowski et al. 2003; Smiljanic et al. 2009). The luminosity bump occurs when the hydrogen-burning shell reaches the chemical discontinuity created by the maximum extent of the convective envelope during the first dredge-up. For many years rotation-induced mixing was thought to be the main mechanism responsible for the abundance anomalies (e.g., Sweigart & Mengel 1979; Charbonnel 1995; Charbonnel et al. 1998; Boothroyd & Sackmann 1999), but more accurate stellar evolution simulations that treat the transport of angular momentum by meridional circulation and shear turbulence self-consistently do not produce enough mixing around the luminosity bump to account for the observed surface abundance variations (Palacios et al. 2006).

A breakthrough occurred when Eggleton et al. (2006) constructed three-dimensional stellar evolution models and discovered the destabilizing role played by the molecular weight inversion that is produced at the external edge of the hydrogen-burning shell by the ^{3}He(^{3}He, $2p$)^{4}He reaction. Charbonnel & Zahn (2007a) pointed out that the first instability to occur under these conditions is a double-diffusive instability called the thermohaline instability (Stern 1960). As the molecular weight gradient increases, the temperature has a stabilizing effect since the timescale for thermal diffusion is shorter than the time it takes for the material to mix.

Stellar evolution models that incorporate thermohaline mixing are able to account for the anomalous $^{12}\mathrm{C}/^{13}\mathrm{C}$ and ^{7}Li abundances that are observed in low-mass stars and predict ^{3}He yields that are significantly reduced compared to standard models (Charbonnel & Zahn 2007a; Denissenkov & Pinsonneault 2008; Eggleton et al. 2008; Cantiello & Langer 2010; Charbonnel & Lagarde 2010; Lagarde et al. 2011). Lagarde et al. (2012) used these stellar yields together with GCE models to predict a modest enrichment of ^{3}He with time that is consistent with H II region observations in the Milky Way disk (see also Balser & Bania 2018).

There are some outstanding issues that remain concerning the treatment of the thermohaline instability just after the luminosity bump on the RGB (see, e.g., Karakas & Lattanzio 2014). The diffusion coefficient is proportional to C, a dimensionless free parameter that is related to the aspect ratio of the "salt" fingers. Charbonnel & Zahn (2007a) use values of $C \sim 1000$ because experiments favor thin fingers instead of blobs (Ulrich 1972). Numerical simulations of thermohaline convection, however, predict a lower value for C than is necessary to solve the ^{3}He problem (e.g., Denissenkov & Merryfield 2011). Rotation may also influence the effectiveness of thermohaline mixing (e.g., Maeder et al. 2013; Sengupta & Garaud 2018).

The fact that a few PNe have estimated ^{3}He/H abundances consistent with standard ^{3}He yields implies that the thermohaline instability is not effective in all low-mass stars. Charbonnel & Do Nascimento (1998) estimate that 4% of red giant stars have $^{12}\mathrm{C}/^{13}\mathrm{C}$ abundance ratios that are consistent with expectations from standard stellar models. GCE models that allow 4% of low-mass stars to produce standard ^{3}He yields (Lagarde et al. 2012) are still consistent with H II region observations (Balser & Bania 2018). Eggleton et al. (2008) suggested that deep mixing of ^{3}He and CNO isotopes is not optional and that this mechanism would destroy most of the ^{3}He produced on the main sequence. Charbonnel & Zahn (2007b) proposed that fossil magnetic fields in red giant stars that are descendants of Ap stars could inhibit thermohaline mixing. In sum, stellar modeling has yet to reach a theoretical consensus concerning the fate of ^{3}He produced by stellar nucleosynthesis.

There is some question, however, whether ^{3}He$^+$ has been detected in any PNe. Using the Green Bank Telescope (GBT), Bania & Balser (2021) have recently shown that the reported

$^3He^+$ detection in NGC 3242 with the MPIfR 100 m, and confirmed with independent observations made with the NRAO 140 Foot telescope (Balser et al. 1999b), is not real. This incorrect result probably stems from systematic errors due to standing waves caused by reflections from the telescope superstructure. Observations of $^3He^+$ from PNe are very challenging since the low ionized mass produces very weak $^3He^+$ intensities that are at the limits of most radio facilities. The clear aperture of the GBT reduced these systematic errors in the spectral baselines by an order of magnitude. Because of these systematic effects in traditionally designed radio telescopes, Bania & Balser (2021) were skeptical of the claimed detection of $^3He^+$ in IC 418 with the NASA Deep Space Station 63 (DSS-63) telescope (Guzman-Ramirez et al. 2016). The lack of any serious tests of the spectral baselines, together with discrepancies in the radio recombination line (RRL) parameters, makes this claimed detection dubious. The only remaining detection of $^3He^+$ in a PN that seems plausible is for J320 observed with the Very Large Array (VLA; Balser et al. 2006). Interferometers have an advantage over single-dish telescopes in that many instrumental spectral baseline effects are removed because the signals between two antennas are correlated. Here we discuss new Jansky Very Large Array (JVLA) observations for the PN J320 made to confirm our previous $^3He^+$ VLA detection.

Table 1
JVLA Observational Summary

Parameters	J320
Project	21A-005
Dates	2021 April 23–2021 May 25
Total time (hr)[a]	29
Configuration	D
R.A. of field center (J2000)	05:05:34.56
Decl. of field center (J2000)	10:42:26.60
LSR central velocity (km s^{-1})	−37.9
Primary beam FWHM (arcmin)	∼5
Synthesized beam FWHM (arcsec)	∼10
Continuum bandwidth (GHz)	2
Line bandwidth (MHz)	16
Number of spectral channels	512
Spectral resolution (kHz)	31.25
Velocity resolution (km s^{-1})	∼1
Velocity span (km s^{-1})	∼500
Flux density/bandpass calibrator	J0542+4951 (3C 147)
Gain calibrator	J0530+1331
Continuum rms (μJy beam^{-1})	25 (bandwidth: 16 MHz)
Line channel rms (μJy beam^{-1})	135 (channel width: 2.5 km s^{-1})

Note.
[a] Wall clock time that includes calibration, slew time, etc.

2. Observations and Data Reduction

Interferometers typically have stable spectral baselines, but they are not perfect. The Balser et al. (2006) J320 VLA observations suffered from three problems: (1) a 3.3 MHz ripple common to all antennas caused by reflections within the waveguide; (2) a limited number of spectral channels and bandwidth, which together provided very few channels for characterizing the spectral baselines; and (3) only one RRL transition available to assess the accuracy of these measurements. The latter two problems were due to limitations with the VLA correlator. Bania & Balser (2021) have shown that tuning to many RRLs simultaneously can be used to assess the accuracy of the spectral baselines and constrain models of the nebula to derive accurate $^3He/H$ abundance ratios.

The JVLA overcomes all three of these problems with the VLA observations. Optical fiber has replaced the old waveguides, and the 3.3 MHz ripple is gone. The JVLA Wideband Interferometric Digital ARchitecture (WIDAR) correlator provides us with an ample number of channels across a large bandwidth to accurately measure the spectral baseline. The flexibility of WIDAR allows us to tune to many RRLs simultaneously to carefully assess the quality of the spectral baselines. For example, adjacent RRLs should have similar line profiles, and we know the intensity ratios of various RRLs in local thermodynamic equilibrium (LTE). Moreover, these RRLs, together with the free–free continuum, can be used to constrain the nebular model required to derive accurate $^3He/H$ abundance ratios.

We therefore used the JVLA at X band (8–10 GHz) in the D configuration to observe $^3He^+$ in the PN J320 to confirm the VLA $^3He^+$ detection. Hereafter, we distinguish between the two J320 $^3He^+$ data sets using the project codes: VLA (AB0794) and JVLA (21A-005). Table 1 summarizes the observations. We observed for a total time of 29 hr to achieve a similar signal-to-noise ratio (S/N) to our previous VLA observations. The half-power beamwidth (HPBW) of the primary beam (field of view) is about 5′ at the $^3He^+$ frequency of 8665.650 MHz, and in the D configuration the synthesized HPBW is about 10″.

We configured the WIDAR correlator so that each of the two 1 GHz basebands was tuned to eight 128 MHz wide spectral windows at full polarization to observe the free–free continuum emission and twelve 16 MHz wide spectral windows at dual polarization to observe various spectral lines. The 128 MHz "continuum" windows each had 64 channels corresponding to a spectral resolution of 2.00 MHz and covering a total of 2 GHz. The 16 MHz "spectral line" windows each had 512 channels corresponding to a spectral resolution of 31.25 kHz (∼1 km s^{-1} at 9 GHz). We sampled the $^3He^+$ hyperfine transition in two spectral windows for redundancy together with these RRL transitions: seven H$n\alpha$, seven H$n\beta$, and eight H$n\gamma$ (see Table 2 for details). Here n is the principal quantum number and α, β, γ correspond to $\Delta n = 1, 2, 3$. The 16 MHz bandwidth provides a velocity span of ∼500 km s^{-1}, sufficient to include the corresponding He$n\alpha$, He$n\beta$, and He$n\gamma$ transitions. The H113β RRL is blended with the H129γ RRL, and therefore these transitions were not observed.

We observed J320 between 2021 April 23 and 2021 May 25 during seven distinct epochs, each with a duration of 4–5 hr. We started each epoch by observing the flux density calibrator J0542+4951 (3C 147), which was also used to set the delays and calibrate the bandpass. We then observed our PN J320 interleaved with observations of the gain calibrator J0530 +1331 every ∼20 minutes.

We use the Wenger Interferometry Software Package (WISP) to calibrate and image our JVLA data (Wenger 2018). WISP is a Python wrapper for the Common Astronomy Software Package (CASA; McMullin et al. 2007). Here we follow the calibration and imaging procedures discussed in Appendix A of Wenger et al. (2019b). The calibration procedures consist of flagging bad data, calculating the calibration solutions, and applying the calibration solutions. This is an iterative process that includes both automatic and manual flagging.

Table 2
JVLA Spectral Windows

Spectral Window	Center Freq.[a] (MHz)	Transition	Bandwidth (MHz)	Channels
Continuum				
1	8057.50009	⋯	128	64
2	8185.50009	⋯	128	64
3	8313.50009	⋯	128	64
4	8441.50009	⋯	128	64
5	8569.50009	⋯	128	64
6	8697.50009	⋯	128	64
7	8825.50009	⋯	128	64
8	8953.50009	⋯	128	64
9	9092.52938	⋯	128	64
10	9220.52938	⋯	128	64
11	9348.52938	⋯	128	64
12	9476.52938	⋯	128	64
13	9604.52938	⋯	128	64
14	9732.52938	⋯	128	64
15	9860.52938	⋯	128	64
16	9988.52938	⋯	128	64
Spectral Line				
17	8665.65	$^3He^+$	16	512
18	8665.65	$^3He^+$	16	512
19	8045.605	H93α	16	512
20	8309.385	H92α	16	512
21	8584.823	H91α	16	512
22	8872.571	H90α	16	512
23	9173.324	H89α	16	512
24	9487.824	H88α	16	512
25	9816.867	H87α	16	512
26	8213.052	H116β	16	512
27	8427.316	H115β	16	512
28	8649.099	H114β	16	512
29	9116.569	H112β	16	512
30	9362.976	H111β	16	512
31	9618.343	H110β	16	512
32	9883.083	H109β	16	512
33	8293.843	H132γ	16	512
34	8483.082	H131γ	16	512
35	8678.122	H130γ	16	512
36	9086.512	H128γ	16	512
37	9300.343	H127γ	16	512
38	9520.936	H126γ	16	512
39	9748.561	H125γ	16	512
40	9983.501	H124γ	16	512

Note. The continuum windows span a total of ∼2 GHz. The spectral line windows have a velocity span of ∼500 km s^{-1} and a spectral resolution of ∼1 km s^{-1}.
[a] Rest frequencies are listed for spectral line windows.

WISP automatically generates clean images from the calibrated visibility data. For the free–free continuum and $^3He^+$ spectral line windows we use the native synthesized HPBW of $9\farcs9 \times 9\farcs2$ when deconvolving the beam from the dirty image. In contrast, for the RRLs we first smooth the images to a common spatial resolution of 12″ since we want to average (stack) RRLs with the same order (e.g., H$n\alpha$, $\Delta n = 1$). These RRLs have different frequencies and therefore different synthesized HPBWs. We denote these stacked spectra as $\langle$H$n\alpha\rangle$, $\langle$H$n\beta\rangle$, and $\langle$H$n\gamma\rangle$. Spectra within the data cubes are smoothed and regridded to a common velocity resolution of 2.5 km s^{-1}. Since typical line widths in PNe are $\gtrsim$ 30 km s^{-1}, we also generate data cubes with a coarse velocity resolution[4] of 11.4 km s^{-1}. The CASA task `TCLEAN` generates the following images and data cubes: (1) a multiscale, multi-frequency synthesis (MS-MFS) continuum image by combining all 16 continuum windows; (2) an MS-MFS image of each continuum and spectral line window; and (3) a multiscale data cube of each spectral line window. Unless noted, the continuum is not subtracted from the spectral line data products.

3. Results

The PN J320, discovered by Jonckheere (1916), is both spatially and kinematically complex. The object has two or three bipolar lobes surrounded by high speed knots, together with a surrounding halo (Harman et al. 2004; Rechy-García et al. 2020). The JVLA MS-MFS radio continuum emission of J320, together with its Hα emission image, is shown in Figure 1. J320 is just resolved by the JVLA, consistent with the Hubble Space Telescope (HST) Hα size of about 10″ (Harman et al. 2004). The complex nature of this PN is therefore not visible in our radio data. The rms noise in the image is 25 μJy beam^{-1}, sufficient to detect the free–free continuum emission from J320 with an S/N > 500. The integrated continuum flux density is 23 mJy at the $^3He^+$ frequency of 8665.65 MHz, consistent with previous VLA results (see Balser et al. 2006).

Figure 2 shows $^3He^+$ and stacked RRL spectra for the spectral pixel (spaxel) in the data cube that corresponds to the brightest region in the continuum image. There is no clear visual evidence of a $^3He^+$ line, but we do detect H II RRL emission in the $\langle$H$n\alpha\rangle$ and $\langle$H$n\beta\rangle$ spectra and perhaps in the $\langle$H$n\gamma\rangle$ spectrum. We therefore fit Gaussian profiles to the H and He RRLs shown by the red curves in the middle panels of Figure 2. Specifically, we simultaneously fit a first-order polynomial and two Gaussian profiles to the entire spectral window. We fix the location of the He component with respect to the H component by −122.47 km s^{-1}, that is, we do not fit for the center velocity of the He component but rather assume the shift produced by the mass of the heavier He nucleus.

Detecting $^3He^+$ emission in PNe is challenging. Instrumental spectral baseline structure can mimic or mask the wide, weak $^3He^+$ spectral transition. We therefore need to rigorously assess the quality of the data and, in particular, the robustness of the nondetection of $^3He^+$ in J320. We employ several statistical techniques to demonstrate that the $^3He^+$ spectrum is consistent with random Gaussian noise.

First, we compare the cumulative distribution functions (CDFs) of the $^3He^+$ and RRL spectra with the CDF expected from theoretical Gaussian noise. The results are shown in Figure 3 for the $^3He^+$, $\langle$H$n\alpha\rangle$, $\langle$H$n\beta\rangle$, and $\langle$H$n\gamma\rangle$ spectra. Here, the spectra have been smoothed to 11.4 km s^{-1}, and the CDF is calculated over the full spectrum. To assess the uncertainty in the CDF distribution, we use bootstrap resampling (Efron 1982). Specifically, we generate 10,000 simulated CDFs, where each distribution consists of M values, the number of data points, that are randomly drawn from the original data with replacement. That is, we replace the original data with the randomly selected data. So the

[4] We specifically chose a velocity resolution of 11.4 km s^{-1} to be consistent with the resolution used by Balser et al. (2006) for their reported $^3He^+$ detection in J320.

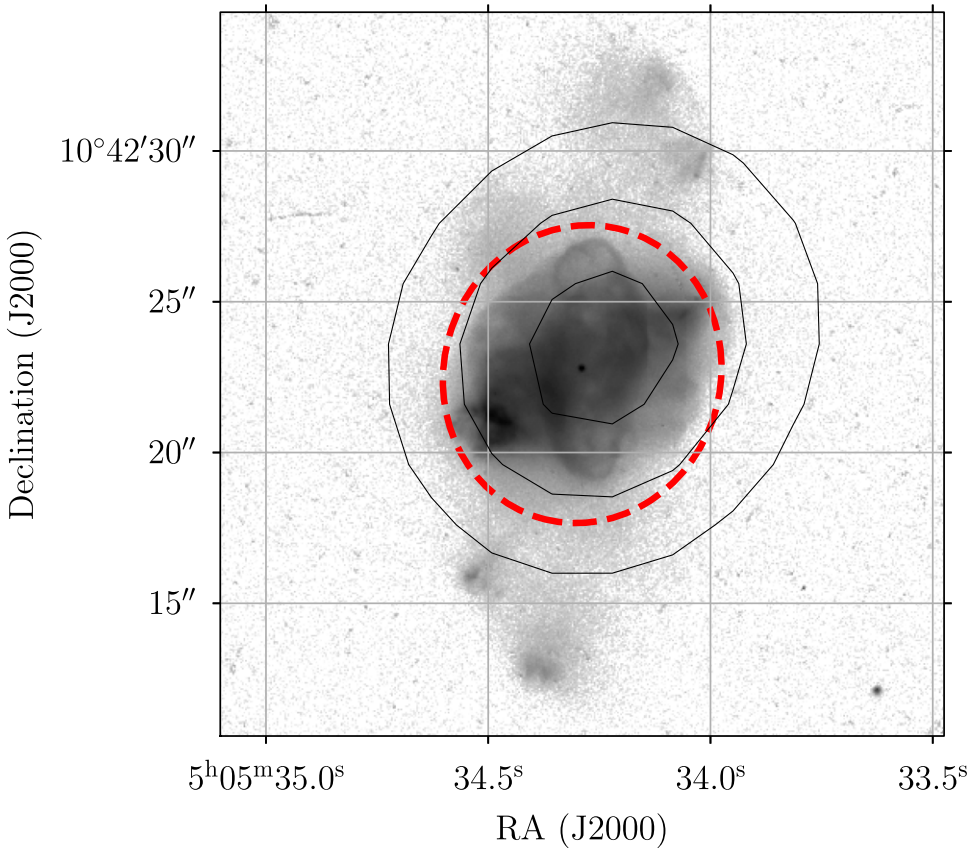

Figure 1. HST Hα and JVLA radio continuum image of J320. Gray scale: HST Hα emission of J320 (see Harman et al. 2004, original observing program: Borkowski PI 6347). Contours: JVLA MS-MFS continuum emission of J320 in the ^{3}He$^+$ spectral window with contour levels at 5, 10, and 15 mJy beam^{-1}. The center frequency is 8665.650 MHz, and the bandwidth is 16 MHz. The rms noise in the image is 25 μJy beam^{-1}. The synthesized HPBW of $9\farcs9 \times 9\farcs2$ is represented by the dashed red ellipse.

simulated distributions will miss some CDF values from the original data and have some duplicates, triplicates, etc. The shaded regions in Figure 3 correspond to the 68% confidence interval ($\pm 1\sigma$) determined by bootstrapping. Visual inspection of the CDFs and their uncertainty indicates that the ^{3}He$^+$ and $\langle \mathrm{H}n\gamma \rangle$ spectra are consistent with noise.

To estimate the significance of this result, we calculate the p-value, the probability of obtaining a result at least as extreme as the value of a test statistic. Here we use the Anderson−Darling (AD) test statistic, which is a weighted sum of the integrated squared difference between the observed CDF and the theoretical Gaussian CDF (see Scholz & Stephens 1987). We use the SciPy implementation of the AD test (see van der Walt et al. 2011). A significance level threshold of 5% is typically used (e.g., Feigelson & Babu 2012), and therefore the spectrum is consistent with random Gaussian noise when the p-value is larger than 0.05. To do this, we run 10,000 simulations where in each simulation we perform the following steps:

1. Generate N random observations of a Gaussian distribution, where N is the same length as the data (or residuals).
2. Calculate the "nominal" AD statistic between the data (or residuals) and this Gaussian distribution.
3. Generate two bootstrap samples of length N from the combined data (or residuals) and random Gaussian observations.
4. Calculate the AD statistic for these two samples and compare this to the nominal value in step 2.
5. Calculate the p-value: the fraction of the time that the AD statistic for the two bootstrapped samples is greater than the nominal AD statistic.

The results are given in Tables 3 and 4 for the ^{3}He$^+$ spectra and stacked RRL spectra, respectively. In Table 3 we list the project, the telescope, the velocity resolution, $\Delta V_{\rm res}$, the rms noise, and the AD p-value. We also summarize the results for the VLA (AB0794) and the combined JVLA (21A-004)/VLA (AB0794) data (see below). The large p-values indicate that the ^{3}He$^+$ spectrum is consistent with noise. This result implies that we have not detected the ^{3}He$^+$ transition and that any instrumental spectral baseline effects are smaller than the expected random Gaussian noise.

In Table 4 we list the RRL order, the velocity resolution, $\Delta V_{\rm res}$, Gaussian fit parameters and S/N for the H and He RRL components, the rms noise, and the AD p-value for the residual and data spectra. The Gaussian fit parameters consist of the peak intensity, S_L, the FWHM line width, ΔV, and the LSR velocity of the peak intensity, $V_{\rm LSR}$. RRLs are only detected with significance in the $\langle \mathrm{H}n\alpha \rangle$ and $\langle \mathrm{H}n\beta \rangle$ spectra. The residual spectra are consistent with random Gaussian noise, implying that our two-component Gaussian fit is sufficient. The S/Ns of the He RRLs are less than 2, and therefore we cannot estimate reliable ^{4}He/H abundance ratios.

The spectral noise in the ^{3}He$^+$ spectral window is consistent with random Gaussian noise. Because previous detections of ^{3}He$^+$ in PNe have been shown to be incorrect (Bania & Balser 2021), we perform several sanity checks on the data.

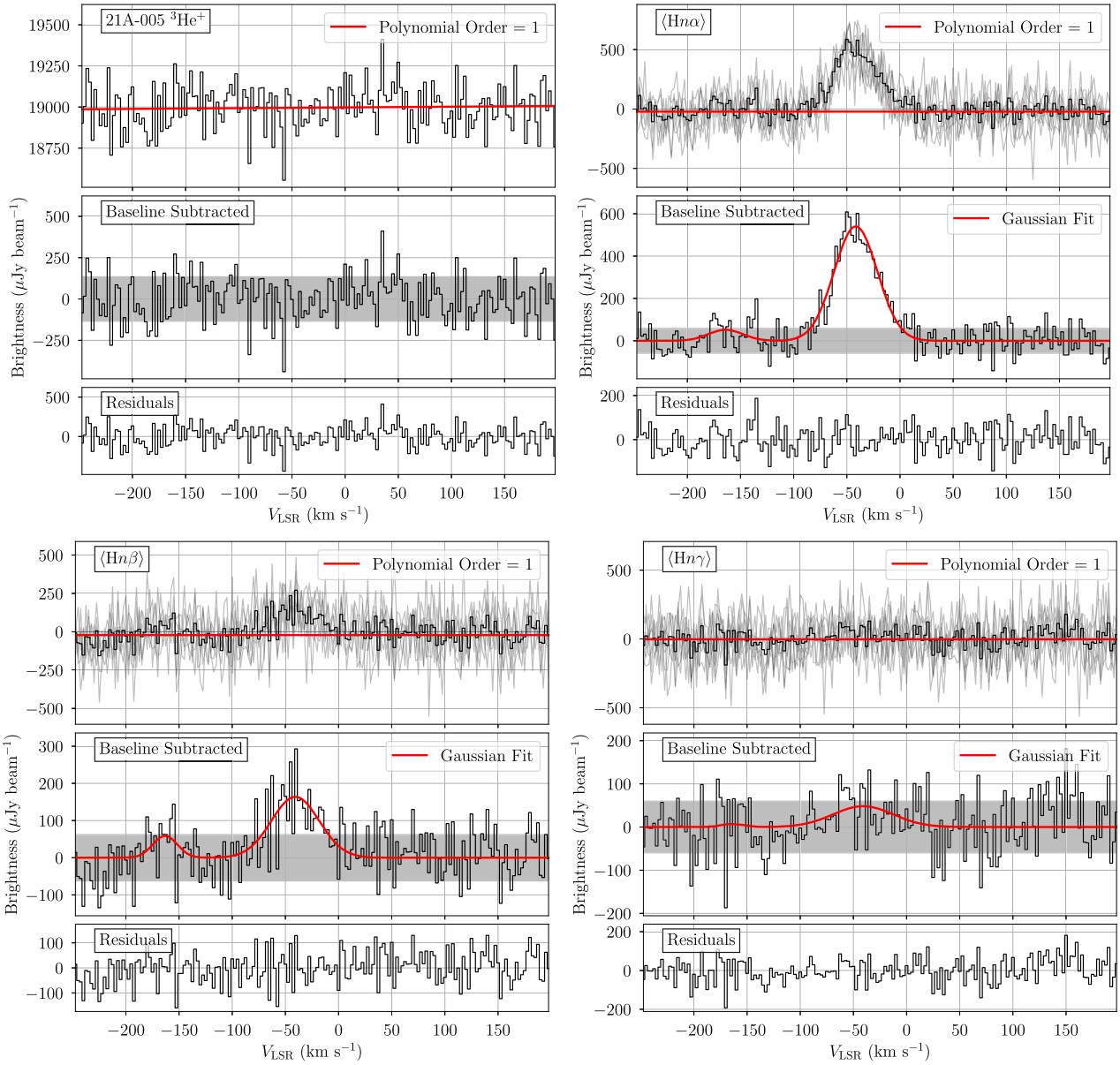

Figure 2. JVLA spectra of J320: ^{3}He$^+$ (top left), ⟨H$n\alpha$⟩ (top right), ⟨H$n\beta$⟩ (bottom left), and ⟨H$n\gamma$⟩ (bottom right). Spectra are extracted from the brightest pixel in the continuum image and are displayed as histograms. The spectra are smoothed and regridded to a velocity resolution of 2.5 km s^{-1}. Top panel: spectrum with the first-order polynomial baseline model (red curve). For the RRL plots the light-gray curves are individual RRL spectra and the black curve corresponds to the stacked RRL spectrum. Middle panel: baseline-subtracted spectrum with a two-component Gaussian fit (red curve) for the RRL spectra only. Here we fit the baseline model and the Gaussian components simultaneously. The He RRL component is assumed to be shifted −122.47 km s^{-1} with respect to the H component. The shaded region represents the 68% confidence interval ($\pm 1\,\sigma$) spectral rms measured in the residual spectrum. Bottom panel: residuals of the Gaussian fit subtracted from the data.

1. *Does the noise integrate down as expected?*. The JVLA exposure calculator tool[5] predicts an rms noise of 51.5 μJy beam^{-1}, assuming a total time of 29 hr and a velocity resolution of 11.4 km s^{-1}. Based on the number of baselines flagged, we estimate an effective integration time of 18.8 hr, increasing the rms noise to 64.0 μJy beam^{-1}. This is roughly consistent with our measured value of 58.8 μJy beam^{-1}.
2. *Do adjacent RRLs behave as expected?* Because RRLs at centimeter wavelengths have large principal quantum numbers, the energy spacing between adjacent RRLs is similar, and therefore these transitions should have similar RRL spectral properties. Moreover, for an optically thin nebula we expect the integrated RRL flux density to increase with frequency: $\int S_\nu d\nu \propto \nu$ (Wilson et al. 2012). Figure 4 shows that both of these expectations are true for the H$n\alpha$ RRLs in J320. Individual H$n\alpha$ RRLs have similar profiles, and the integrated flux density increases linearly with frequency to within the uncertainty. A power-law fit to the data yields an exponent of 1.79 ± 0.84. This is a large deviation from the expected exponent of 1.0 for an optically thin nebula, but consistent to within the uncertainties.
3. *Are the RRLs in LTE?* There have been non-LTE effects detected for RRLs in PNe, but in general we expect centimeter-wavelength RRLs to be close to LTE (see, e.g., Bania & Balser 2021). In LTE we expect the

[5] See go.nrao.edu/ect.

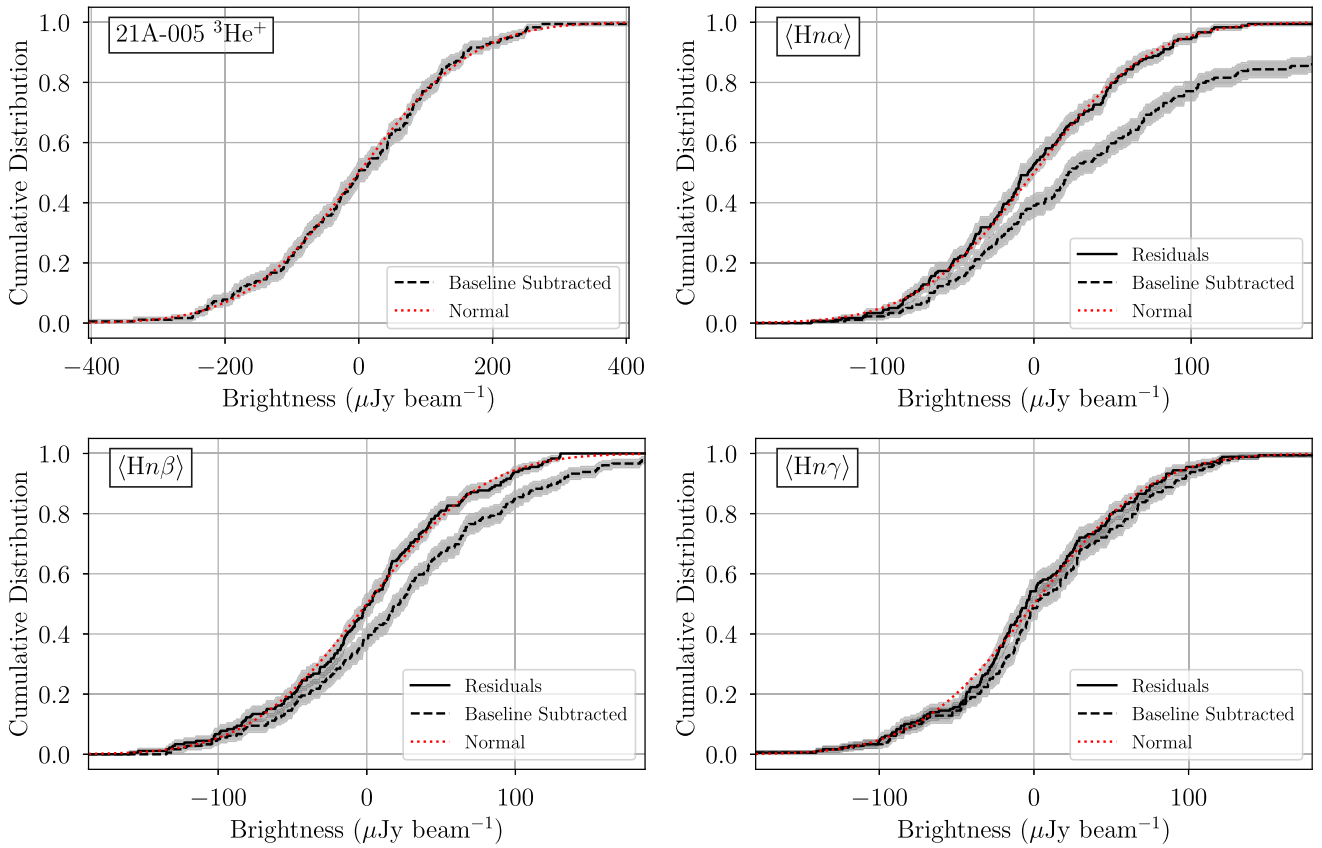

Figure 3. JVLA cumulative distribution functions of the spectra in Figure 2: ^{3}He$^+$ (top left), ⟨H$n\alpha$⟩ (top right), ⟨H$n\beta$⟩ (bottom left), and ⟨H$n\gamma$⟩ (bottom right). The dashed black curve is the CDF of the baseline-subtracted spectrum (middle panel of Figure 2), the solid black curve is the CDF of the residual spectrum (bottom panel of Figure 2), and the red dotted curve is the CDF of theoretical Gaussian noise with an rms given by the residual spectrum. For the ^{3}He$^+$ spectrum the residual curve is equivalent to the baseline-subtracted curve and therefore is not shown. The shaded regions correspond to the 68% confidence interval ($\pm 1\sigma$) determined by bootstrapping. These figures show significant detections of ⟨H$n\alpha$⟩ and ⟨H$n\beta$⟩ emission but only upper limits for ⟨H$n\gamma$⟩ and ^{3}He$^+$ emission.

Table 3
JVLA (21A-005) and VLA (AB0794) ^{3}He$^+$ Results

Project	Telescope	$\Delta V_{\rm res}$ (km s^{-1})	rms Noise[a] (μJy beam^{-1})	AD p-value
21A-005	JVLA	2.5	134.7	0.670
21A-005	JVLA	11.4	58.8	0.625
AB0794	VLA	8.0	127.0	0.605
AB0794	VLA	11.4	113.3	0.600
Combine	JVLA/VLA	8.0	68.2	0.665
Combine	JVLA/VLA	11.4	61.1	0.668

Note.
[a] The spectral noise in the data cube.

following integrated intensity ratios: H114β/H91α = 0.274 and H130γ/H91α = 0.126 (Bania & Balser 2021). From Table 4 we measure ⟨H$n\beta$⟩/⟨H$n\alpha$⟩ = 0.335 ± 0.067 and ⟨H$n\gamma$⟩/⟨H$n\alpha$⟩ = 0.125 ± 0.071. So within the uncertainties the RRL emission is consistent with LTE excitation in J320.

Many PNe, including J320, contain diffuse halos that can be detected with deep Hα observations. Since the intensity of free–free and RRL emission is proportional to $\int n_e^2\, d\ell$, these tracers are not a very sensitive probe of the halo. In contrast, the intensity of the ^{3}He$^+$ transition is proportional to $\int n_e\, d\ell$, and thus the halo could contribute significantly to the ^{3}He$^+$ emission (see Balser et al. 1997). To increase our sensitivity to ^{3}He$^+$ emission, we therefore follow Balser et al. (2006) and integrate ^{3}He$^+$ emission both over the line profile and spatially around J320. Specifically, we first integrate over the expected FWHM line width of the ^{3}He$^+$ transition, that is, we produce a channel-integrated image from the ^{3}He$^+$ data cube. Using this image, we then spatially integrate over concentric rings centered on J320.

Figure 5 shows the results of this analysis for the JVLA data. In the left panel we plot the cumulative free–free continuum flux density as a function of radius. The free–free emission levels off beyond about 15″, that is, we do not detect any halo emission with our radio data. This is expected given the low emission measure probed by Hα emission in PN halos. In the right panel we plot the cumulative, channel-integrated ^{3}He$^+$ line flux density as a function of radius. No ^{3}He$^+$ emission is detected. The noise, shown by the shaded regions for the data and residuals, increases with radius since we are integrating over a noisy signal. The darker shaded region is where the noise envelopes of the data and residual curves overlap.

To compare our results with Balser et al. (2006), we reanalyze their VLA data (project AB0794) using WISP with the same procedures as for our JVLA data for consistency. We also combine the VLA and JVLA data to increase our sensitivity. Since the VLA correlator was limited to spectral windows with 31 channels over a 6.25 MHz bandwidth, we first smooth our JVLA data to the same spectral resolution of 8.0 km s^{-1}. Spectra and CDFs are shown in Figure 6. There is a hint of a double-peaked ^{3}He$^+$ profile in the reprocessed VLA data, which is consistent with the results in Balser et al. (2006, Figure 7). But this feature is

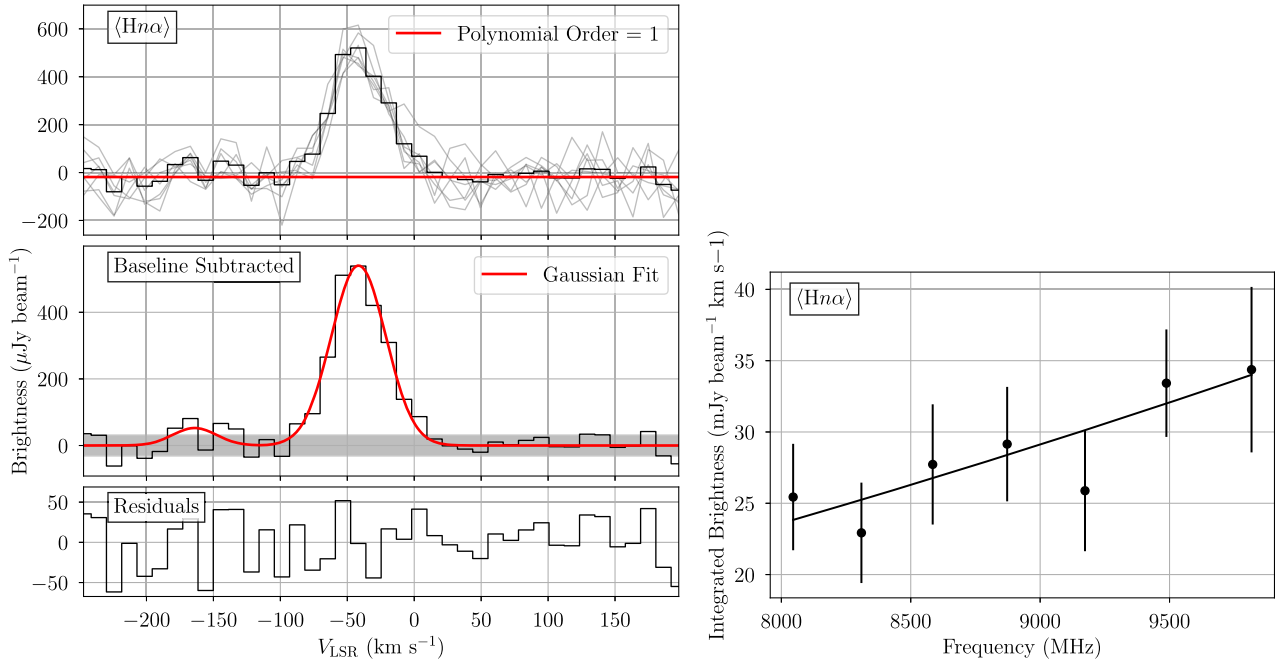

Figure 4. Analysis of individual H$n\alpha$ RRL transitions for the JVLA data. Left panel: spectra of seven RRLs (H87α–H93α) and the stacked $\langle$H$n\alpha\rangle$ RRL spectrum in bold (top), the $\langle$H$n\alpha\rangle$ RRL spectrum after the removal of a spectral baseline (middle), and the residuals (bottom). Right panel: integrated H$n\alpha$ brightness as a function of frequency. The solid line is a power-law fit to the points with an exponent of 1.79 ± 0.84.

Table 4
JVLA (21A-005) Radio Recombination Line Results

		Hydrogen				Helium				AD p-value	
Δn	$\Delta V_{\rm res}$ (km s^{-1})	S_L (μJy beam^{-1})	ΔV (km s^{-1})	$V_{\rm LSR}$ (km s^{-1})	S/N	S_L (μJy beam^{-1})	ΔV (km s^{-1})	S/N	rms Noise (μJy beam^{-1})	Residuals	Data
1	2.5	539.9 ± 19.8	47.9 ± 2.1	-41.6 ± 0.8	28.05	51.9 ± 22.1	38.2 ± 19.4	2.41	59.0	0.665	0.000
1	11.4	540.3 ± 23.7	48.0 ± 2.5	-41.6 ± 1.0	24.98	52.6 ± 26.4	38.5 ± 23.1	2.18	31.1	0.543	0.021
2	2.5	163.7 ± 20.0	52.9 ± 7.8	-40.7 ± 2.8	8.45	58.7 ± 27.6	27.0 ± 15.0	2.16	62.4	0.622	0.010
2	11.4	163.8 ± 19.4	53.1 ± 7.6	-40.7 ± 2.7	9.25	58.0 ± 26.6	27.9 ± 15.1	2.37	26.8	0.688	0.024
3	2.5	48.2 ± 17.2	66.8 ± 29.2	-40.8 ± 11.0	2.91	7.2 ± 28.3	23.7 ± 110.3	0.26	60.0	0.578	0.296
3	11.4	48.6 ± 20.0	72.2 ± 36.3	-35.2 ± 11.1	2.70	24.6 ± 39.5	15.0 ± 28.8	0.62	31.7	0.597	0.398

Note. We follow Lenz & Ayres (1992) to calculate the S/N.

not present in the JVLA data or in the combined data set. Moreover, all spectra are consistent with random Gaussian noise (see the CDFs in Figure 6 and the AD p-values in Table 3).

The spectral line rms noise in the reprocessed VLA data is almost two times higher than the JVLA data using the coarse velocity resolution data cubes with $\Delta V_{\rm res} = 11.4$ km s^{-1} (see Table 3). There are three factors that account for most of this difference: (1) the lower system noise in the JVLA receivers produces a system equivalent flux density (SEFD) of ~250 Jy at X band compared to ~310 Jy for the VLA; (2) the JVLA WIDAR correlator efficiency is 0.93 for the 8-bit samplers, whereas the 3-level VLA correlator had an efficiency of 0.78; and (3) the VLA data require significant flagging due to bad data resulting in an effective integration time of 13.5 hr, whereas the cleaner JVLA data set has an effective integration time of 18.8 hr. In total, these three differences account for a factor of 1.7 in rms sensitivity between the VLA and JVLA data sets. Thus, combining the VLA data with the JVLA data does not significantly change the measured rms noise.

Why did Balser et al. (2006) *claim a* $^3He^+$ *detection?* Their ^{3}He$^+$ spectrum toward the peak continuum emission is consistent with our results: no significant ^{3}He$^+$ detection. The difference arises when generating the cumulative, channel-integrated flux density, where they achieve an S/N of ~9 (see Figure 8 in Balser et al. 2006). The main reason for the discrepancy stems from performing a continuum subtraction using the few available channels in the VLA correlator to define the line-free regions. This produces a poor spectral baseline fit that artificially amplifies the "noise" bumps visible in the single spectrum centered on J320. The magnitude of the ^{3}He$^+$ signal increases when calculating the cumulative, channel-integrated flux density. In contrast, the JVLA data have ample channels to define the line-free region; moreover, since the line data are not limited by dynamic range, a continuum subtraction is not necessary. By processing the VLA data in the same way as Balser et al. (2006), we can reproduce their results.

3.1. J320 NEBULA Model

Deriving a limit for the ^{3}He/H abundance ratio in J320 requires a model of the nebular structure for this PN. Balser et al. (2006) modeled J320 as a two-component nebula consisting of a bright shell and a diffuse, extended halo. They

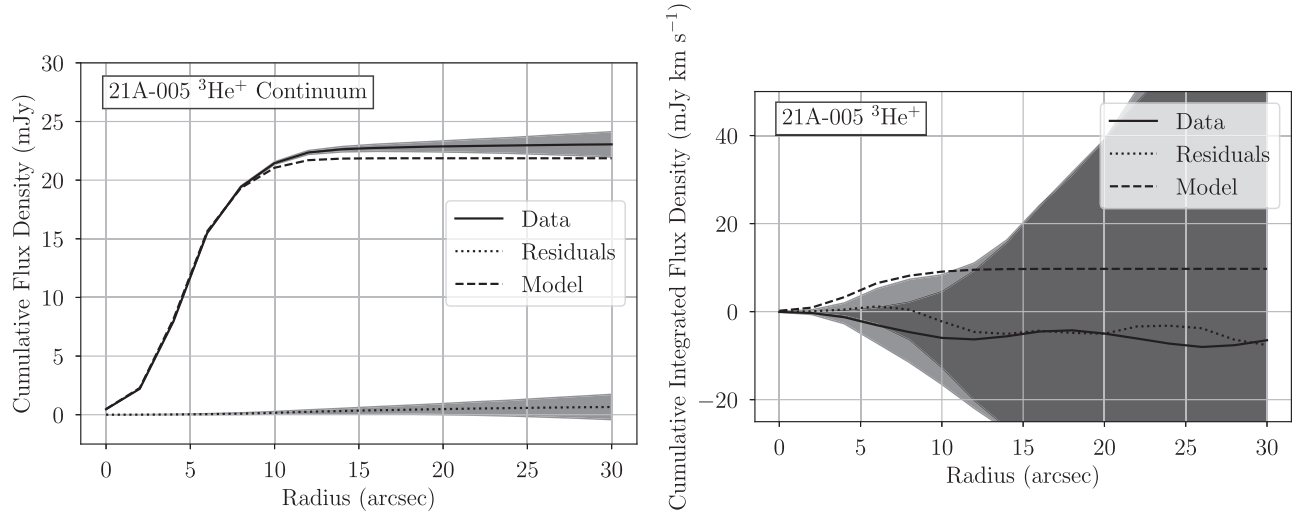

Figure 5. Spatially integrated free–free continuum (left) and ^{3}He$^+$ line (right) flux densities as a function of radius for the JVLA (21A-005) data. For the ^{3}He$^+$ line emission we first integrate over spectral channels and then spatially around J320. Data (solid curves): the continuum MS-MFS image of the ^{3}He$^+$ spectral line window (left) and the channel-integrated ^{3}He$^+$ spectrum (right). Both images were smoothed to 12″ resolution. Residuals (dotted curves): the continuum residual cumulative flux density is measured in the MS-MFS residual image (left), and the ^{3}He$^+$ spectral line residual cumulative integrated flux density is measured in the line-free channels (right). The shaded regions represent the 1σ uncertainties determined from the residual (continuum) or line-free channels (^{3}He$^+$ spectral line). Model (dashed curves): results of a similar analysis for the NEBULA model free–free continuum image and ^{3}He$^+$ spectral line cube (see Section 3.1).

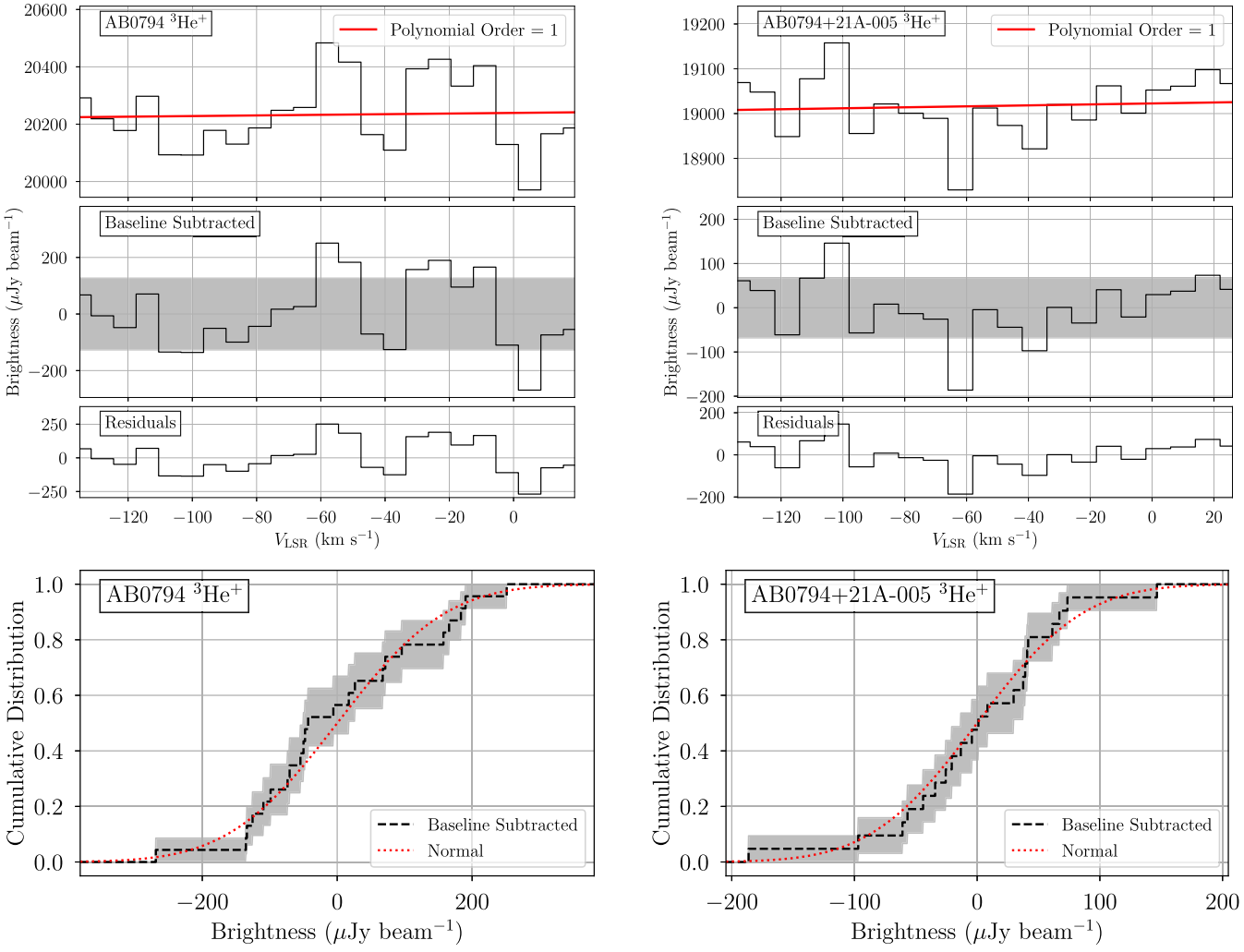

Figure 6. J320 ^{3}He$^+$ spectra (top) and CDFs (bottom) using the VLA (project AB0794; left) and the combined VLA and JVLA data (projects AB0794 and 21A-005; right). Spectra are smoothed and regridded to a velocity resolution of 8.0 km s^{-1}. See Figures 2 and 3 for details. Combining the VLA and JVLA J320 data does not lead to a ^{3}He$^+$ detection.

Table 5
J320 NEBULA Model Parameters

Component	$\theta_{\rm inner}$ (arcsec)	$\theta_{\rm outer}$ (arcsec)	$V_{\rm exp}$ (km s^{-1})	T_e (K)	n_e (cm^{-3})	(^{4}He$^+$/H$^+$)	(^{4}He^{++}/H$^+$)	(^{3}He$^+$/H$^+$)
Shell	0.1	7.0	16.0	12,500	2100	0.10	0.00	2.75×10^{-3}
Halo	7.0	25.0	16.0	12,500	10	0.10	0.00	2.75×10^{-3}

Note. We adopt a distance of 3.26 kpc to J320 based on Gaia DR2 parallaxes (Chornay & Walton 2020).

used the numerical radiative transfer code NEBULA (Balser 1995; Balser et al. 1999a; Balser & Bania 2018) to calculate synthetic spectra of the free–free continuum, RRL, and ^{3}He$^+$ emission from this model nebula. Specifically, NEBULA produces a continuum image and spectral line data cubes.

Here, we use more recent optical and infrared data, together with our sensitive JVLA radio data, to constrain the physical properties of J320. We adopt a distance of 3.26 kpc based on parallax observations from Gaia DR2 (Chornay & Walton 2020). J320 is morphologically complex, but there exists a brighter shell with an angular diameter of $\sim 7''$ embedded within a larger halo of $\sim 25''$ (Harman et al. 2004). The angular size of the inner boundary of the shell is difficult to discern from the optical images, so we assume $0\farcs1$. The helium ionization structure is taken from optical recombination lines, where we assume that the doubly ionized helium is negligible (Costa et al. 2004). For an optically thin nebula in LTE the radio recombination line-to-continuum ratio is an accurate measure of the electron temperature that is independent of density (see, e.g., Wenger et al. 2019a). Using the H91α RRL, we derive $T_{\rm e} = 12{,}500$ K, consistent with results derived from optical collisionally excited lines (e.g., Milingo et al. 2002; Costa et al. 2004). Using infrared collisionally excited lines of sulfur, Pagomenos et al. (2018) derive an electron density of $n_e = 3350 \pm 600\,{\rm cm}^{-3}$. This produces radio continuum emission brighter than observed with the JVLA, so we reduce this value to $n_e = 2100\,{\rm cm}^{-3}$ to be consistent with our radio observations. The infrared and radio data are not probing the same volume for this complex nebula; therefore, reducing the density is justified.

The RRL line widths in J320 are broadened by Doppler motions, consisting of both thermal and nonthermal components, together with expansion of the nebula. Harman et al. (2004) measured bipolar lobes expanding with a velocity of $V_{\rm exp} = 46$ km s^{-1}, but this value is unlikely to be representative of our RRL emission, which arises from the entire volume of ionized gas. We therefore adopt an expansion velocity of $V_{\rm exp} = 16$ km s^{-1} based on Hα emission of the entire shell (Rechy-García et al. 2020). The thermal motions are determined by the electron temperature, which we derive to be $T_e = 12{,}500$ K (see above). The nonthermal motions, thought to be caused by turbulence, are constrained by the observed JVLA line widths. That is, we increase the model turbulent velocity until the synthetic RRL line widths are consistent with the observed line widths.

The NEBULA model physical parameters for J320 are summarized in Table 5. Listed are the nebular component, the inner and outer angular sizes, the expansion velocity, the electron temperature, the electron density, and the helium ionic abundances. The physical parameters of the halo are not well determined because the low density produces weak emission lines. We therefore assume that the halo has the same expansion velocity, electron temperature, and helium ionization structure as the shell. Balser et al. (2006) used the ^{3}He$^+$ and continuum emission distribution to constrain the halo density and ^{3}He/H abundance ratio. Since we do not detect ^{3}He$^+$ with the improved JVLA observations, we arbitrarily set the density to a low value of $n_e = 10\,{\rm cm}^{-3}$. A ^{3}He/H abundance ratio of 2.75×10^{-3} by number produces a limit to our JVLA observations (see below).

We analyze the NEBULA data products of J320 using the same methods as for our JVLA data. The model brightness distribution is convolved with a Gaussian beam with HPBW of $12''$. Spectra of the H91α RRL and ^{3}He$^+$ transition toward the peak continuum emission in J320 are shown in Figure 7. The synthetic H91α profile is a reasonable fit by eye to the JVLA data. This is expected since the model electron temperature and density were constrained using the JVLA H91α line-to-continuum ratio and the free–free radio continuum emission centered on J320. The NEBULA model produces a ^{3}He$^+$ line intensity that is about 2–3 times the rms noise of the JVLA data.

We also spatially integrate the synthetic free–free continuum and ^{3}He$^+$ line flux densities as a function of radius to increase the sensitivity. The model results are shown as the dashed line in Figure 5. The free–free continuum emission in our model is a good fit to the data, with a cumulative continuum flux density that is slightly less than the value derived from our JVLA continuum observations. The cumulative, channel-integrated modeled ^{3}He$^+$ emission is larger than the observational uncertainties at smaller radii. Since the contribution of the ^{3}He$^+$ emission arising from the halo may be significant, and we are unable to put stringent constraints on the physical properties of the halo, we cannot derive an accurate ^{3}He/H abundance ratio limit for J320. Nevertheless, the synthetic ^{3}He$^+$ profile in Figure 7, which is 2–3 times the rms spectral noise, produces a limit of $^3{\rm He/H} \leqslant 2.75 \times 10^{-3}$ by number.

4. Discussion

There is ample evidence that stars undergo extra mixing beyond convection as a physical process to stir material in their interiors. There are a variety of tracers, including ^{3}He, ^{7}Li, ^{12}C/^{13}C, etc., observed in stars and PNe whose abundances are inconsistent with standard stellar evolution models that only include convection. For low-mass stars the best candidates for this extra mixing process are rotation-induced mixing and the thermohaline instability. Rotation alone is not sufficient to explain the abundance anomalies (Palacios et al. 2006), but models that include both of these extra mixing processes predict abundances at different stellar evolutionary states that are broadly consistent with observations (e.g., Charbonnel & Lagarde 2010). Moreover, these extra mixing processes resolve the "^{3}He problem" (e.g., Lagarde et al. 2012; Balser & Bania 2018).

One criticism of thermohaline mixing is that although we might expect all low-mass stars to destroy their ^{3}He by processing it into ^{4}He, there are several PNe with ^{3}He/H abundance ratios consistent with standard stellar yields (e.g., Eggleton et al. 2008). Charbonnel & Zahn (2007b) suggested that strong

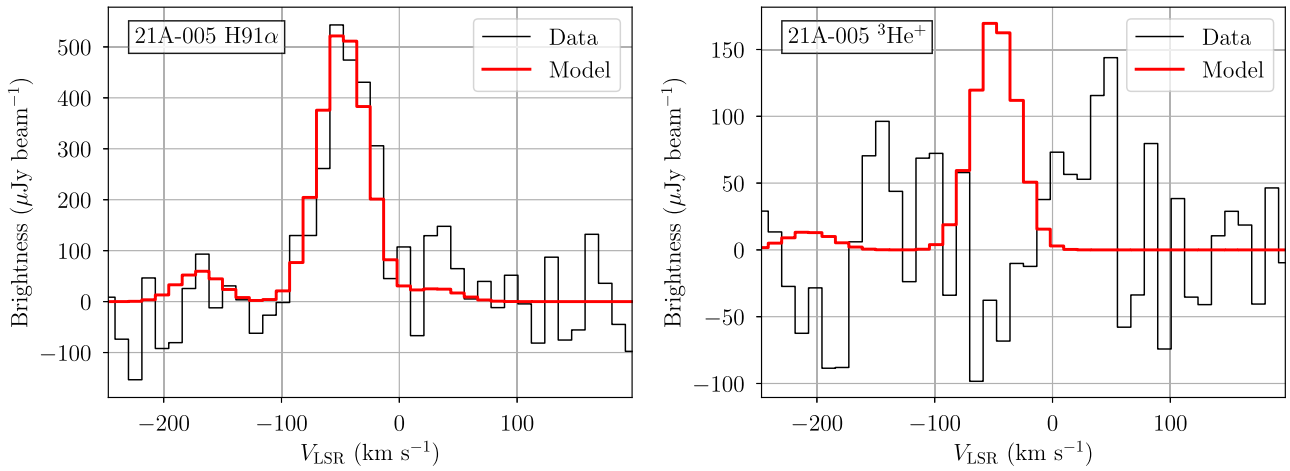

Figure 7. J320 NEBULA model synthetic spectra of the H91α RRL and the ^{3}He$^+$ transition. JVLA (project 21A-005) spectra are shown as black histograms for comparison. The data and model spectral line cubes have been smoothed to a 12″ angular resolution. Left panel: H91α RRL band. The model H91α RRL is a reasonably good fit to the data. The He91α RRL (near $V_{LSR} \sim -165$ km s^{-1}) and H154ϵ RRL (near $V_{LSR} \sim 26$ km s^{-1}) are included in the NEBULA model but are too weak to be detected with the JVLA. Right panel: ^{3}He$^+$ transition band. The model ^{3}He$^+$ intensity is about 2–3 times the JVLA rms noise (see Table 3). The H171η RRL (near $V_{LSR} \sim -210$ km s^{-1}) is included in the model but too weak to be detected with the JVLA.

magnetic fields could inhibit thermohaline mixing. They posited that Ap-type stars, which have stronger magnetic fields than classical A-type stars, could maintain their magnetic field strength as they evolve into RGB stars, when the thermohaline instability is important. But this may no longer be necessary since the two most significant ^{3}He$^+$ detections in PNe, NGC 3242 and J320, have now been shown to be incorrect.

Do all low-mass stars undergo extra mixing? This is still an open question. Charbonnel & Do Nascimento (1998) estimated that 96% of low-mass stars undergo extra mixing on the RGB. Using HIPPARCOS parallaxes, they identified a sample of 191 stars that have passed the luminosity bump in their evolution. It is at this evolutionary stage when these extra mixing mechanisms are expected to be active. Additional processing of material, however, could occur later in the evolution of low-mass stars. To answer this extra-mixing question, we must therefore determine abundances in objects whose material has been fully processed by stellar evolution: PNe.

Here we focus on ^{3}He and the carbon isotopic ratio ^{12}C/^{13}C in PNe to explore whether extra mixing occurs in all low-mass stars. One major difficulty with using PN abundances to constrain stellar evolution models is that the progenitor mass, also called the initial mass, M_i, is required. This is because we need to compare abundances derived from observations in PNe with stellar evolution models that depend strongly on the initial stellar mass. Determining the progenitor mass is a two-step process. First, the PN central star mass or final mass, M_f, must be determined. This is typically done by placing the central star on an H-R diagram for comparison with evolutionary tracks from stellar models (e.g., Stanghellini et al. 1993), but there are other methods (see Gorny et al. 1997). Therefore, the PN central star distance is needed to derive the luminosity. Second, a semiempirical initial-to-final mass relation (IFMR) is used to calculate the initial mass given the final mass. The IFMR is calibrated by carefully measuring the properties of white dwarfs in open clusters, where the age and therefore cooling time can be estimated (e.g., Canton 2018). Recently, Marigo et al. (2020) have shown that the IFMR is not monotonic and unfortunately there is a kink in the relationship where low-mass stars reside.

Since we need final masses to determine the initial masses, we therefore search for PNe in the literature with ^{3}He/H or ^{12}C/^{13}C abundance ratios that also have an estimate of the central star mass. We then calculate a range in M_i using the IFMR from three different sources (Canton 2018; Cummings et al. 2018; Marigo et al. 2020). We must first generate a grid of possible initial masses between 0.83 and 7.22 $M_\odot$ with an increment of 0.01 $M_\odot$. We then determine the range of initial masses that are consistent with the PN final mass assuming a 10% error in M_f. The methods used to derive these IFMRs are similar, but the white dwarf samples and detailed analyses are different (for a comparison of these IFMRs see Canton et al. 2021). Our calculated ranges in M_i therefore provide an estimate of the uncertainty and include the kink in the IFMR discovered by Marigo et al. (2020).

4.1. ^{3}He/H Abundance Ratio in Planetary Nebulae

Detecting ^{3}He$^+$ in PNe is very challenging since the mass of ionized gas in these nebulae is small, producing very weak emission-line intensities. Typically, a detection of ^{3}He$^+$ with current radio facilities translates into an abundance ratio of ^{3}He/H $\gtrsim 10^{-3}$. This limit is either consistent with or larger than that predicted by standard stellar models. Therefore, ^{3}He/H upper limits are usually not particularly useful, but there are some exceptions (see below). Table 6 summarizes the properties of the three PNe with claimed ^{3}He$^+$ detections. Listed are the ^{3}He/H abundance ratio and estimates of the final and initial stellar masses. Since IC 418 is a carbon star, the progenitor mass likely has a higher value for the lower limit than the number listed in Table 6, that is, $M_i \gtrsim 1.5\,M_\odot$ (Morisset & Georgiev 2009). Bania & Balser (2021) have clearly demonstrated that the previously claimed detection of ^{3}He$^+$ in NGC 3242 is incorrect, and therefore their limits are shown in Table 6. Using the JVLA, we have demonstrated here that the claimed detection of ^{3}He$^+$ in J320 is also incorrect, and therefore we include the limits determined in Section 3. Finally, we list the range of ^{3}He/H abundance ratios derived by Guzman-Ramirez et al. (2016) for IC 418.

We conclude that there is no longer strong evidence from PN ^{3}He$^+$ observations that any low-mass stars fail to undergo extra mixing. Figure 8 plots the ^{3}He/H abundance ratio as a function of progenitor mass, where the points correspond to abundances derived from observations and the curves correspond to yields from stellar evolution models. For low-mass stars the expected

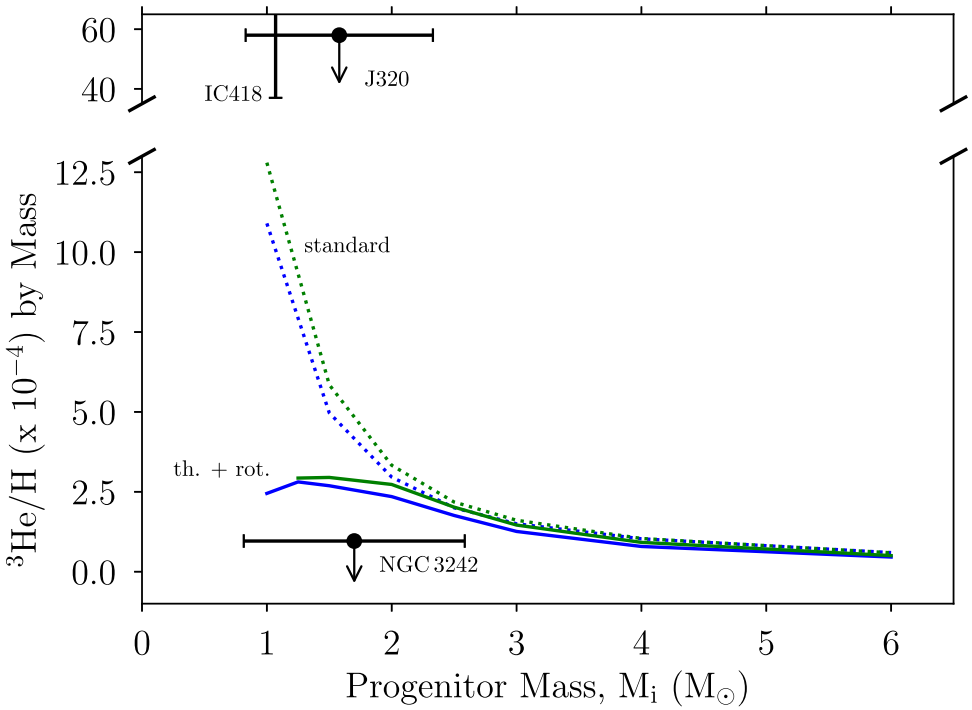

Figure 8. ^{3}He/H abundance ratios in PNe based on observations (points) and stellar evolution models (curves) as a function of progenitor mass. ^{3}He/H limits are given for NGC 3242 (Bania & Balser 2021) and J320 (this paper). The lower bounds of the ^{3}He/H abundance ratio are shown for IC 418 (Guzman-Ramirez et al. 2016), where the progenitor mass is shifted by -0.5 $M_\odot$ for clarity. Models are from Lagarde et al. (2011), where the dotted curves assume standard stellar evolution and the solid curves include thermohaline and rotation-induced mixing after the second dredge-up. The blue and green curves correspond to metallicity $Z = 0.004$ and 0.014, respectively.

Table 6
^{3}He/H Abundances in Planetary Nebulae

		(^{3}He/H) 10^{-4}			M_f ($M_\odot$)			
PN	Alias	by Number	by Mass	Ref.	Value	Error	Ref.	M_i ($M_\odot$)
190.3–17.7	J320	⩽27.5	⩽58	This paper	0.575	⋯	G97	0.83−2.33
261.0 + 32.0	NGC 3242	⩽0.45	⩽0.96	B21	0.615	⋯	S20	0.83−2.57
215.2–24.2	IC 418	17 − 58	37 − 123	G16	0.573	⋯	G97	0.83−2.32

Note. Listed are the ^{3}He/H abundance ratios, the PN central star mass (or final mass M_f), and the PN progenitor mass (or initial mass M_i). We convert the ^{3}He/H abundance ratio by number to mass fraction assuming a ^{4}He/H abundance ratio by number of 0.1 and a metallicity of $Z = 0.0061$ for NGC 3242 and $Z = 0.0122$ for J320 and IC 418 (see Bania & Balser 2021).
References: B21: Bania & Balser 2021; G16: Guzman-Ramirez et al. 2016; G97: Gorny et al. 1997; S20: Stanghellini et al. 2020.

^{3}He abundances are reduced when thermohaline mixing is included. The ^{3}He/H upper limit for J320 is significantly larger than all models and is therefore not very significant. The very deep GBT ^{3}He$^+$ observations toward NGC 3242, however, produce a significant ^{3}He/H upper limit that is clearly not consistent with standard stellar yields. (We do not include a similar limit for the PN NGC 6543 since Bania & Balser 2021 deem that this limit is not very reliable.) The lower range of the IC 418 ^{3}He/H abundance ratio derived by Guzman-Ramirez et al. (2016) is higher than all models. If this abundance is accurate, then it does not support extra mixing. As discussed by Bania & Balser (2021), however, there are serious issues with these data, and this detection needs to be confirmed.

4.2. $^{12}C/^{13}C$ Abundance Ratio in Planetary Nebulae

There are several different tracers used to derive the ^{12}C/^{13}C abundance ratio in PNe. The brightest is the millimeter-wavelength rotational transition of CO (e.g., Palla et al. 2000). There are three problems in deriving accurate ^{12}C/^{13}C ratios using CO: (1) opacity variations, (2) chemical fractionation, and (3) selective dissociation (Stahl et al. 2008). For high densities ^{12}CO will become optically thick, and therefore the derived ^{12}C/^{13}C ratios will be underestimated. This can be mitigated by observing at least two transitions of CO and using radiative transfer models to determine the opacity (e.g., Balser et al. 2002). Since the molecular gas in PNe is warm (20−50 K), fractionation should be small (Ziurys et al. 2020). But Saberi et al. (2020) see variations in ^{12}C/^{13}C from CO due to selective dissociation in the outflows of AGB stars and suggest that HCN is a better tracer. Since ^{12}CO is more efficiently shielded than ^{13}CO, the derived ^{12}C/^{13}C ratios can be overestimated when using CO. Nevertheless, observations of multiple molecular tracers (e.g., CO, HCN, CN, HCO$^+$, etc.) to determine ^{12}C/^{13}C abundances produce results that are consistent to within the uncertainties, but there are some exceptions (Ziurys et al. 2020).

A less sensitive tracer of ^{12}C/^{13}C abundance is the C III] multiplet near 1908 Å, which has an $F = 1/2$–$1/2$ transition

Table 7
$^{12}C/^{13}C$ Abundances in Planetary Nebulae

PN	Alias	$^{12}C/^{13}C$				M_f ($M_\odot$)			M_i ($M_\odot$)
		Value	Error	Ref.	Tracer	Value	Error	Ref.	
010.1 + 00.7	NGC 6537	2.4	0.30	Z20	HCN	0.80	0.10	M05	1.8 – 4.2
036.1–57.1	NGC 7293	12.	5.4	Z20	HCO^+	0.71	···	S20	1.6 – 3.3
037.7–34.5	NGC 7009	⩾ 5.6	···	R04	C III]	0.60	···	G97	0.83 – 2.5
041.8–02.9	NGC 6781	20.	1.0	P00	CO	0.82	···	S20	2.8 – 4.5
060.8–03.6	NGC 6853	⩾ 46.	···	P00	CO	0.71	···	S20	1.6 – 3.3
063.1 + 13.9	NGC 6720	9.5	1.6	B02	CO	0.66	···	S20	1.3 – 2.9
084.9–03.4	NGC 7027	31.	0.62	B02	CO	0.67	0.030	P00	1.4 – 3.0
089.8–05.1	IC 5117	14.	1.0	P00	CO	0.56	0.020	P00	0.83 – 2.2
093.4 + 05.4	NGC 7008	⩾ 12.	···	P00	CO	0.60	···	G97	0.83 – 2.5
103.2 + 00.6	M2-51	15.	1.0	P00	CO	0.63	0.090	P00	0.98 – 2.7
106.5–17.6	NGC 7662	⩾ 6.5	···	R04	C III]	0.68	···	S20	1.5 – 3.0
189.8 + 07.7	M1-7	20.	1.8	B02	CO	0.59	···	S97	0.83 – 2.4
215.6 + 03.6	NGC 2346	22.	2.7	B02	CO	0.63	0.020	P00	0.98 – 2.7
226.7 + 05.6	M1-16	2.2	0.030	B02	CO	0.56	0.020	P00	0.83 – 2.2
228.8 + 05.3	M1-17	22.	1.0	P00	CO	0.55	0.050	P00	0.83 – 1.5
234.8 + 02.4	NGC 2440	1.6	0.50	Z20	HCN	0.66	0.070	M19	1.3 – 2.9
261.0 + 32.0	NGC 3242	⩾ 14.	···	R04	C III]	0.61	···	S20	0.83 – 2.6
294.6 + 04.7	NGC 3918	⩾ 9.9	···	R04	C III]	0.62	···	G97	0.88 – 2.6
319.6 + 15.7	IC 4066	20.	3.0	C92	CO	0.76	···	G97	1.7 – 3.7
342.1 + 10.8	NGC 6072	12.	3.0	Z20	HCN	0.91	···	G97	3.4 – 5.4
342.1 + 27.5	Me2-1	⩾ 6.9	···	R04	C III]	0.72	···	G97	1.6 – 3.4

Note. Listed are the isotopic carbon ratio by number, $^{12}C/^{13}C$, the PN central star mass (or final mass M_f), and the PN progenitor mass (or initial mass M_i). We only include significant limits ($^{12}C/^{13}C \geqslant 5$).

References: B02: Balser et al. 2002; C92: Cox et al. 1992; G97: Gorny et al. 1997; M05: Matsuura et al. 2005; M19: Miller et al. 2019; P00: Palla et al. 2000; R04: Rubin et al. 2004; S97: Stasińska et al. 1997; S20: Stanghellini et al. 2020; Z20: Ziurys et al. 2020.

near 1909.6 Å that is only allowed for ^{13}C (Clegg et al. 1997). Most studies using this ultraviolet transition toward PNe, however, only produce limits to $^{12}C/^{13}C$ (see Rubin et al. 2004).

In Table 7, we list PNe with $^{12}C/^{13}C$ abundance ratios from the literature that have estimates of the central star mass, M_f. For PNe with $^{12}C/^{13}C$ ratios determined by different tracers we favor HCN, CN, or HCO^+ instead of CO owing to potential issues with selective dissociation. For PNe with multiple $^{12}C/^{13}C$ ratios based only on CO we favor those that use radiative transfer models to derive the $^{12}C/^{13}C$ abundance. We only include PNe that have significant limits: $^{12}C/^{13}C \geqslant 5$ (see below). There are two independent observations of the C III] multiplet transition in the well-known PN NGC 3242 made using HST and the International Ultraviolet Explorer. These data yield abundance ratios of $^{12}C/^{13}C \geqslant 38$ (Palla et al. 2002) and $^{12}C/^{13}C \geqslant 14$ (Rubin et al. 2004), respectively, by number. Inspection of the spectrum from Palla et al. (2002, Figure 1) suggests that the quoted upper limit of $^{12}C/^{13}C \geqslant 38$ is too high. The peak-to-peak fluctuations in the residual spectrum are about 0.2, suggesting a 3σ limit in the ^{13}C transition of about 0.2 ergs cm^{-2} s^{-1} $arcsec^{-2}$, a factor of 10 larger than quoted. We therefore list the limit of $^{12}C/^{13}C \geqslant 14$ derived by Rubin et al. (2004) in Table 7.

Figure 9 plots the $^{12}C/^{13}C$ abundance ratio by mass as a function progenitor mass. Here we convert the $^{12}C/^{13}C$ abundance ratios listed in Table 7 from number density to mass fraction to compare with stellar evolution models. This requires multiplying the $^{12}C/^{13}C$ abundance ratios by the small factor of 12/13. The results span a wide range of values but are concentrated at values of $^{12}C/^{13}C \leqslant 20$ and progenitor masses between 1 and 3 $M_\odot$. As expected, the progenitor masses are rather uncertain, with error bars on the order of 1 $M_\odot$. For comparison the predictions of the $^{12}C/^{13}C$ ratio from stellar evolution models are shown in the bottom panel. The different curves correspond to yields using standard models and those that include extra mixing from the thermohaline instability and rotation. For low-mass stars there is a significant difference in the expected $^{12}C/^{13}C$ ratio between these models, whereas for higher-mass stars the models predict $^{12}C/^{13}C \sim 20$, unless there is significant rotation.

In Figure 10, we combine the $^{12}C/^{13}C$ results from observations with the predictions from models. Since these stellar evolution models do not include the combined effect of third dredge-up, hot bottom burning, and thermohaline mixing for more massive stars, we only show PNe with progenitor masses less than 2 $M_\odot$. The very low $^{12}C/^{13}C$ ratio of 2.2 for M1-16 suggests additional mixing beyond that included in the models. But otherwise interpreting Figure 10 is difficult given the large uncertainty in progenitor masses. For example, a PN with $^{12}C/^{13}C \sim 20$ is consistent with the standard model for a progenitor mass of 1 $M_\odot$, but the interpretation is inconclusive if the progenitor mass is 2 $M_\odot$.

There is one PN, however, that appears consistent with the standard model: M1-17. There are, however, some potential problems with M1-17. First, as discussed above, $^{12}C/^{13}C$ abundance ratios can be overestimated owing to selective dissociation. Observations of HCN, or similar tracers, should therefore be made toward M1-17 to confirm the high $^{12}C/^{13}C$ values. Second, since most authors do not include an error for the central star mass, we have assumed a nominal uncertainty of 10%. If we had chosen a 20% uncertainty, then the progenitor mass range for M1-17 would be 0.83–2.5 $M_\odot$, making the results harder to interpret. Nevertheless, Palla et al. (2000) did include an error of about 10% for the M1-17 central star mass (see Table 7). One major source of error in determining the central star mass is

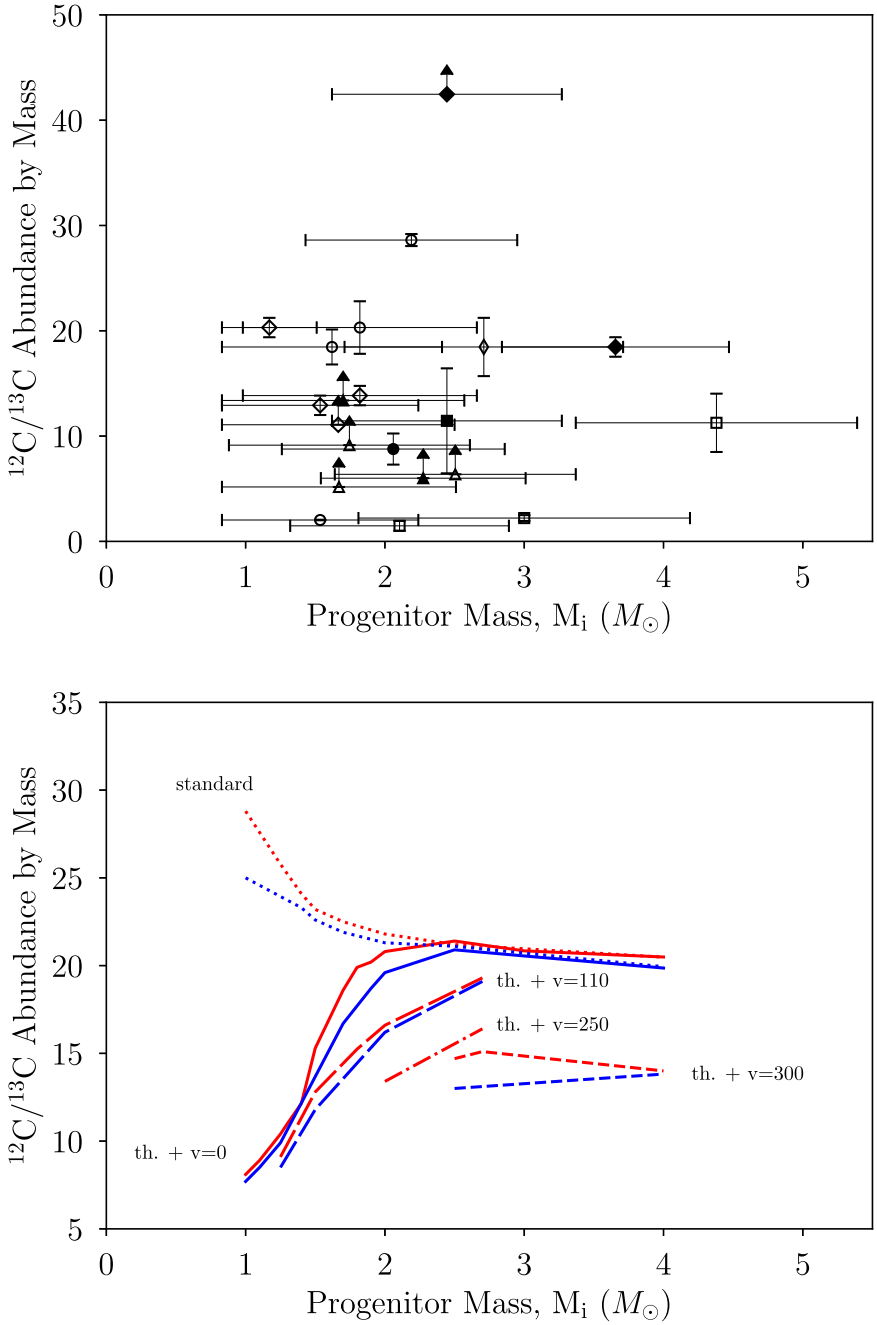

Figure 9. $^{12}C/^{13}C$ abundance ratios in PNe as a function of progenitor mass. Top: $^{12}C/^{13}C$ ratios from millimeter molecular transitions (thin diamond: Cox et al. 1992; diamond: Palla et al. 2000; circle: Balser et al. 2002; square: Ziurys et al. 2020) and ultraviolet C III transitions (triangle; Rubin et al. 2004). Filled symbols have central stellar masses derived with accurate parallax-determined distances (Stanghellini et al. 2020). Bottom: model $^{12}C/^{13}C$ predictions from Charbonnel & Lagarde (2010) for standard stellar evolution models (dotted) and models that include thermohaline mixing (solid). Also shown are models that include both thermohaline and rotation-induced mixing with various initial stellar rotation velocities (long-dashed line: $v = 110$ km s^{-1}; dashed–dotted line: $v = 250$ km s^{-1}; dashed line: $v = 300$ km s^{-1}). The red curves correspond to $^{12}C/^{13}C$ ratios at the tip of the RGB, whereas the blue curves are $^{12}C/^{13}C$ ratios at the end of the second dredge-up.

the distance. Gaia parallaxes do exist for some PN central stars, but alas not for M1-17. Nevertheless, PN parallaxes from Gaia have been used to calibrate a Galactic PN distance scale based on the correlation between nebular physical radius and Hβ surface brightness (Stanghellini et al. 2020). Applying this new Galactic PN distance scale to M1-17 would yield more accurate estimates for the progenitor mass.

We conclude that, based on the $^{12}C/^{13}C$ abundance ratios in PNe, there is evidence that some low-mass stars fail to undergo extra mixing. More work is required, however, to confirm this. In particular, additional observations of HCN or similar tracers toward PNe to derive $^{12}C/^{13}C$ abundance ratios are needed. In addition, unless parallaxes are available, the new Galactic PN distance scale should be used to derive PN progenitor masses.

5. Conclusions

For many decades there has been evidence that extra mixing beyond convection must occur in low-mass stars. Observations of ^{7}Li, $^{12}C/^{13}C$, C/O, and other tracers on the RGB isolate this extra mixing to just after the star reaches the luminosity bump, when the

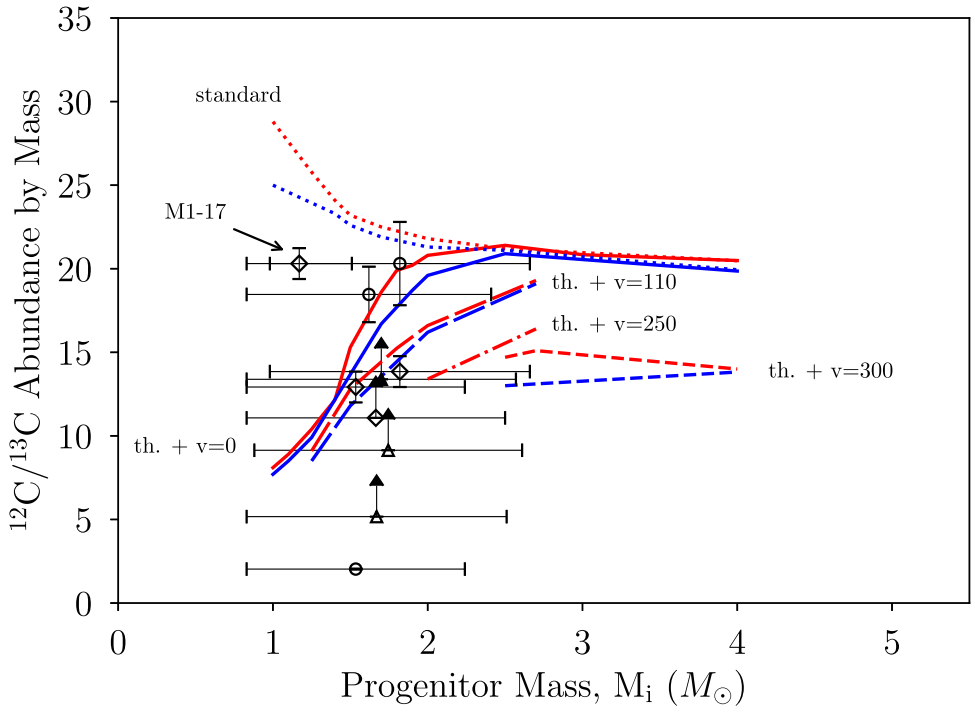

Figure 10. $^{12}C/^{13}C$ abundance ratios in PNe based on observations (symbols) and models (curves) as a function of progenitor mass. See Figure 9 for details. We only include low-mass progenitor stars ($M_i \leqslant 2$). All PNe with progenitor masses derived using parallax distances (filled symbols) require extra mixing processes to account for their $^{12}C/^{13}C$ abundance ratios. The PN M1-17 is labeled in the plot.

hydrogen-burning shell reaches the chemical discontinuity created by the maximum extent of the convective envelope during the first dredge-up. The two most likely candidates for this extra mixing are rotational-induced mixing and the thermohaline instability.

Observations of ^{3}He in PNe provide an important constraint to mixing mechanisms in stars since they probe abundances in places that have been fully processed by stellar evolution. Standard stellar evolution models that only include convection as a way to mix material inside stars predict the production of significant amounts of ^{3}He. But GCE models that use these standard ^{3}He yields produce ^{3}He/H abundance ratios in the ISM that are much higher than are observed. This "^{3}He problem" can be resolved if most stars undergo extra mixing as predicted by models that include the thermohaline instability. Yet there are a few PNe (NGC 3242, J320, and IC 418) with ^{3}He/H abundance ratios consistent with the standard models, indicating that not all low-mass stars undergo extra mixing.

Recent GBT observations of NGC 3242, however, reveal that the detection of $^3He^+$ in this PN is not real. A mere detection of $^3He^+$ is at the limit of most radio facilities, and therefore each claimed detection must be carefully scrutinized. Moreover, the detection of $^3He^+$ in IC 418 is suspect given the lack of any serious tests of the spectral baselines, together with discrepancies in the measured RRL parameters.

Here we observe $^3He^+$ at 8665.65 MHz in J320 made with the JVLA in the D configuration to confirm a previous $^3He^+$ detection with the older VLA and to produce a definitive result. Our more sensitive observations do not detect the $^3He^+$ transition with an rms noise of 58.8 μJy beam^{-1}. We estimate an abundance ratio limit for J320 of $^3\mathrm{He/H} \leqslant 2.75 \times 10^{-3}$ by number using the radiative transfer code NEBULA. Based on ^{3}He data, there is no longer strong evidence that some low-mass stars do not undergo extra mixing.

We also explore extra mixing by using the $^{12}C/^{13}C$ abundance ratio in PNe. Taking $^{12}C/^{13}C$ data from the literature, we find one PN, M1-17, that is consistent with standard stellar yields, indicating that at least some low-mass stars do not undergo extra mixing. The high $^{12}C/^{13}C$ ratio of 22 in M1-17 needs to be confirmed, however, by observations of HCN or similar tracers instead of CO, which is susceptible to selective dissociation.

We thank an anonymous referee for valuable comments that improved this paper. We thank Letizia Stanghellini for discussions about planetary nebulae and the initial-to-final mass relation. Emmanuel Momjian provided technical information about the VLA and JVLA. The National Radio Astronomy Observatory is a facility of the National Science Foundation operated under cooperative agreement by Associated Universities, Inc. This work is supported by NSF grant AST1714688 to T.M.B. This research has made use of NASA's Astrophysics Data System Bibliographic Services.

Facilities: VLA.

Software: Astropy (Astropy Collaboration et al. 2013), CASA (McMullin et al. 2007), Matplotlib (Hunter 2007), NumPY & SciPy (van der Walt et al. 2011), WISP (Wenger 2018), NEBULA (Balser & Bania 2018).

ORCID iDs

Dana S. Balser https://orcid.org/0000-0002-2465-7803
Trey V. Wenger https://orcid.org/0000-0003-0640-7787
T. M. Bania https://orcid.org/0000-0003-4866-460X

References

Balser, D. S. 1995, PhD thesis, Boston Univ.
Balser, D. S., & Bania, T. M. 2018, NEBULA: Radiative transfer code of ionized nebulae at radio wavelengths, Astrophysics Source Code Library ascl:1809.009

Balser, D. S., Bania, T. M., Brockway, C. J., Rood, R. T., & Wilson, T. L. 1994, ApJ, 430, 667
Balser, D. S., Bania, T. M., Rood, R. T., & Wilson, T. L. 1997, ApJ, 483, 320
Balser, D. S., Bania, T. M., Rood, R. T., & Wilson, T. L. 1999a, ApJ, 510, 759
Balser, D. S., Goss, W. M., Bania, T. M., & Rood, R. T. 2006, ApJ, 640, 360
Balser, D. S., McMullin, J. P., & Wilson, T. L. 2002, ApJ, 572, 326
Balser, D. S., Rood, R. T., & Bania, T. M. 1999b, ApJL, 522, L73
Bania, T. M., & Balser, D. S. 2021, ApJ, 910, 73
Bania, T. M., Balser, D. S., Rood, R. T., Wilson, T. L., & LaRocque, J. M. 2007, ApJ, 664, 915
Bania, T. M., Balser, D. S., Rood, R. T., Wilson, T. L., & Wilson, T. J. 1997, ApJS, 113, 353
Bania, T. M., Rood, R. T., & Balser, D. S. 2002, Natur, 415, 54
Bania, T. M., Rood, R. T., & Wilson, T. L. 1987, ApJ, 323, 30
Boesgaard, A. M., & Steigman, G. 1985, ARA&A, 23, 319
Boothroyd, A. I., & Sackmann, I. J. 1999, ApJ, 510, 232
Cantiello, M., & Langer, N. 2010, A&A, 521, A9
Canton, P. 2018, PhD thesis, Univ. of Oklahoma
Canton, P. A., Williams, K. A., Kilic, M., & Bolte, M. 2021, AJ, 161, 169
Charbonnel, C. 1995, ApJL, 453, L41
Charbonnel, C., Brown, J. A., & Wallerstein, G. 1998, A&A, 332, 204
Charbonnel, C., & Do Nascimento, J. D. J. 1998, A&A, 336, 915
Charbonnel, C., & Lagarde, N. 2010, A&A, 522, A10
Charbonnel, C., & Zahn, J. P. 2007a, A&A, 467, L15
Charbonnel, C., & Zahn, J. P. 2007b, A&A, 476, L29
Chornay, N., & Walton, N. A. 2020, A&A, 638, A103
Clegg, R. E. S., Storey, P. J., Walsh, J. R., & Neale, L. 1997, MNRAS, 284, 348
Costa, R. D. D., Uchida, M. M. M., & Maciel, W. J. 2004, A&A, 423, 199
Cox, P., Omont, A., Huggins, P. J., Bachiller, R., & Forveille, T. 1992, A&A, 266, 420
Cummings, J. D., Kalirai, J. S., Tremblay, P. E., Ramirez-Ruiz, E., & Choi, J. 2018, ApJ, 866, 21
Cyburt, R. H., Fields, B. D., & Olive, K. A. 2008, JCAP, 2008, 012
Denissenkov, P. A., & Merryfield, W. J. 2011, ApJL, 727, L8
Denissenkov, P. A., & Pinsonneault, M. 2008, ApJ, 684, 626
Efron, B. 1982, The Jackknife, the Bootstrap and other Resampling Plans (Philadelphia, PA: Society for Industrial and Applied Mathematics)
Eggleton, P. P., Dearborn, D. S. P., & Lattanzio, J. C. 2006, Sci, 314, 1580
Eggleton, P. P., Dearborn, D. S. P., & Lattanzio, J. C. 2008, ApJ, 677, 581
Feigelson, E., & Babu, G. 2012, Modern Statistical Methods for Astronomy: With R Applications (Cambridge: Cambridge Univ. Press)
Galli, D., Palla, F., Ferrini, F., & Penco, U. 1995, ApJ, 443, 536
Galli, D., Stanghellini, L., Tosi, M., & Palla, F. 1997, ApJ, 477, 218
Gilroy, K. K. 1989, ApJ, 347, 835
Goldwire, H. C., & Goss, W. M. J. 1967, ApJ, 149, 15
Gorny, S. K., Stasińska, G., & Tylenda, R. 1997, A&A, 318, 256
Gratton, R. G., Sneden, C., Carretta, E., & Bragaglia, A. 2000, A&A, 354, 169
Güsten, R., Wiesemeyer, H., Neufeld, D., et al. 2019, Natur, 568, 357
Guzman-Ramirez, L., Pineda, J. E., Zijlstra, A. A., Stancliffe, R., & Karakas, A. 2013, MNRAS, 432, 793
Guzman-Ramirez, L., Rizzo, J. R., Zijlstra, A. A., et al. 2016, MNRAS, 460, L35
Harman, D. J., Bryce, M., López, J. A., Meaburn, J., & Holloway, A. J. 2004, MNRAS, 348, 1047
Hogan, C. J. 1995, ApJL, 441, L17
Hunter, J. D. 2007, CSE, 9, 90
Jonckheere, R. 1916, Obs, 39, 134
Karakas, A. I., & Lattanzio, J. C. 2014, PASA, 31, e030
Lagarde, N., Charbonnel, C., Decressin, T., & Hagelberg, J. 2011, A&A, 536, A28
Lagarde, N., Romano, D., Charbonnel, C., et al. 2012, A&A, 542, A62
Lenz, D. D., & Ayres, T. R. 1992, PASP, 104, 1104
Luck, R. E. 1994, ApJS, 91, 309
Maeder, A., Meynet, G., Lagarde, N., & Charbonnel, C. 2013, A&A, 553, A1
Mahaffy, P. R., Donahue, T. M., Atreya, S. K., Owen, T. C., & Niemann, H. B. 1998, SSRv, 84, 251
Marigo, P., Cummings, J. D., Curtis, J. L., et al. 2020, NatAs, 4, 1102
Matsuura, M., Zijlstra, A. A., Gray, M. D., Molster, F. J., & Waters, L. B. F. M. 2005, MNRAS, 363, 628
McMullin, J. P., Waters, B., Schiebel, D., Young, W., & Golap, K. 2007, in ASP Conf. Ser., 376, Astronomical Data Analysis Software and Systems XVI, ed. R. A. Shaw, F. Hill, & D. J. Bell (San Francisco, CA: ASP), 127
Milingo, J. B., Henry, R. B. C., & Kwitter, K. B. 2002, ApJS, 138, 285
Miller, T. R., Henry, R. B. C., Balick, B., et al. 2019, MNRAS, 482, 278
Morisset, C., & Georgiev, L. 2009, A&A, 507, 1517
Novick, R., & Cummins, E. D. 1958, PhRv, 111, 822
Olive, K. A., Rood, R. T., Schramm, D. N., Truran, J., & Vangioni-Flam, E. 1995, ApJ, 444, 680
Pagomenos, G. J. S., Bernard-Salas, J., & Pottasch, S. R. 2018, A&A, 615, A29
Palacios, A., Charbonnel, C., Talon, S., & Siess, L. 2006, A&A, 453, 261
Palla, F., Bachiller, R., Stanghellini, L., Tosi, M., & Galli, D. 2000, A&A, 355, 69
Palla, F., Galli, D., Marconi, A., Stanghellini, L., & Tosi, M. 2002, ApJL, 568, L57
Pilachowski, C., Sneden, C., Freeland, E., & Casperson, J. 2003, AJ, 125, 794
Predmore, C. R., Goldwire, H. C. J, & Walters, G. K. 1971, ApJL, 168, L125
Rechy-García, J. S., Guerrero, M. A., Duarte Puertas, S., et al. 2020, MNRAS, 492, 1957
Romano, D., Tosi, M., Matteucci, F., & Chiappini, C. 2003, MNRAS, 346, 295
Rood, R. T., Bania, T. M., & Wilson, T. L. 1984, ApJ, 280, 629
Rood, R. T., Bania, T. M., & Wilson, T. L. 1992, Natur, 355, 618
Rood, R. T., Steigman, G., & Tinsley, B. M. 1976, ApJL, 207, L57
Rood, R. T., Wilson, T. L., & Steigman, G. 1979, ApJL, 227, L97
Rubin, R. H., Ferland, G. J., Chollet, E. E., & Horstmeyer, R. 2004, ApJ, 605, 784
Saberi, M., Olofsson, H., Vlemmings, W. H. T., et al. 2020, A&A, 638, A99
Sargent, A. W. L. W., & Jugaku, J. 1961, ApJ, 134, 777
Scholz, F. W., & Stephens, M. A. 1987, J. Am. Stat. Assoc., 82, 918
Seling, T. V., & Heiles, C. 1969, ApJL, 155, L163
Sengupta, S., & Garaud, P. 2018, ApJ, 862, 136
Smiljanic, R., Gauderon, R., North, P., et al. 2009, A&A, 502, 267
Stahl, O., Casassus, S., & Wilson, T. 2008, A&A, 477, 865
Stanghellini, L., Bucciarelli, B., Lattanzi, M. G., & Morbidelli, R. 2020, ApJ, 889, 21
Stanghellini, L., Corradi, R. L. M., & Schwarz, H. E. 1993, A&A, 279, 521
Stasińska, G., Gorny, S. K., & Tylenda, R. 1997, A&A, 327, 736
Stern, M. E. 1960, Tell, 12, 1972
Sweigart, A. V., & Mengel, J. G. 1979, ApJ, 229, 624
Syunyaev, R. A. 1966, AZh, 43, 1237
Townes, C. H. 1957, in Radio Astronomy, Proc. of the 4th IAU Symp., ed. H. C van de Hulst, 4 (Cambridge: Cambridge Univ. Press), 92
Ulrich, R. K. 1972, ApJ, 172, 165
van der Walt, S., Colbert, S. C., & Varoquaux, G. 2011, CSE, 13, 22
Weiss, A., Wagenhuber, J., & Denissenkov, P. A. 1996, A&A, 313, 581
Wenger, T. V. 2018, WISP: Wenger Interferometry Software Package, Astrophysics Source Code Library ascl:1812.001
Wenger, T. V., Balser, D. S., Anderson, L. D., & Bania, T. M. 2019a, ApJ, 887, 114
Wenger, T. V., Dickey, J. M., Jordan, C. H., et al. 2019b, ApJS, 240, 24
Wiedenbeck, M. E., Bučík, R., Mason, G. M., et al. 2020, ApJS, 246, 42
Wilson, T. L., Rohlfs, K., & Huttemeister, S. 2012, Tools of Radio Astronomy (5th edn; Berlin: Springer)
Ziurys, L. M., Schmidt, D. R., & Woolf, N. J. 2020, ApJL, 900, L31